

A dynamics-based density profile for dark haloes – II. Fitting function

Benedikt Diemer^{*}

Department of Astronomy, University of Maryland, College Park, MD 20742, USA

Accepted 2022 December 18. Received 2022 November 15; in original form 2022 May 6

ABSTRACT

The density profiles of dark matter haloes are commonly described by fitting functions such as the NFW or Einasto models, but these approximations break down in the transition region where halos become dominated by newly accreting matter. Here we present a simple, accurate new fitting function that is inspired by the asymptotic shapes of the separate orbiting and infalling halo components. The orbiting term is described as a truncated Einasto profile, $\rho_{\text{orb}} \propto \exp[-2/\alpha (r/r_s)^\alpha - 1/\beta (r/r_t)^\beta]$, with a five-parameter space of normalization, physically distinct scale and truncation radii, and α and β , which control how rapidly the profiles steepen. The infalling profile is modelled as a power law in overdensity that smoothly transitions to a constant at the halo centre. We show that these formulae fit the averaged, total profiles in simulations to about 5% accuracy across almost all of an expansive parameter space in halo mass, redshift, cosmology, and accretion rate. When fixing $\alpha = 0.18$ and $\beta = 3$, the formula becomes a three-parameter model that fits individual halos better than the Einasto profile on average. By analogy with King profiles, we show that the sharp truncation resembles a cut-off in binding energy.

Key words: methods: numerical – dark matter – large-scale structure of Universe

1 INTRODUCTION

The shapes that make up the cosmic web of dark matter are generally too complex to be described mathematically (e.g. Doroshkevich & Shandarin 1978; Bond et al. 1996). However, the densest structures, or haloes, collapse into relatively uniform and roughly spherical shapes. Describing haloes analytically is critical because they contain about half the dark and most of the observable baryons in the Universe. The most common description are spherically averaged density profiles, which conveniently summarize simulation results (Dubinski & Carlberg 1991), serve as the basis of galaxy formation models (Wechsler & Tinker 2018), underlie descriptions of large-scale structure via the halo model (Cooray & Sheth 2002), are used to fit observed profile data (e.g., Courteau et al. 2014), and provide a parameter space in which to compare such observations to theory and simulations (e.g., Umetsu 2020; Eckert et al. 2022).

To facilitate these applications, numerous fitting functions have been proposed, although many were originally intended for galaxies rather than haloes. The three-parameter Einasto (1965, 1969) profile features a slope that smoothly steepens with radius and thus contains a finite mass. Many later proposals are essentially double power laws that smoothly transition between two slopes around a scale radius, r_s (Dehnen 1993). This group includes the profiles of Jaffe 1983 (with inner slope -2 and outer slope -4), Hernquist 1990 (-1 and -4), Burkert 1995 (0 and -3), Navarro et al. 1995, 1996, 1997 (hereafter NFW, -1 and -3), and Moore et al. 1999 (-1.5 and -3 , see also Ghigna et al. 2000). Numerous studies have found the extra parameter of the Einasto profile to be justified by a superior fit to simulation results (Navarro et al. 2004, 2010; Graham et al. 2006; Merritt et al.

2006; Gao et al. 2008; Stadel et al. 2009; Ludlow et al. 2011; Wang et al. 2020). Naturally, the fit of power-law models can be improved by adding more slope parameters (Zhao 1996; Dekel et al. 2017; Freundlich et al. 2020). Finally, an entire different class of models can be derived by assuming a distribution of particle energies and computing the corresponding density structure (King 1966; Shapiro et al. 1999; Hjorth & Williams 2010; Pontzen & Governato 2013).

All of these models were intended to fit density profiles out to roughly the virial radius, a focus that makes sense given that galaxy formation happens at much smaller radii. For example, one of the key debates has been whether the central slope of the profiles is characteristic of a flat core or a power-law cusp (e.g., de Blok 2010; Teyssier et al. 2013; Di Cintio et al. 2014; Genina et al. 2018). A second reason is that the nature of the profiles changes fundamentally beyond the virial radius, where the profile becomes dominated by particles that are falling into the halo for the first time. In this transition region, the profile shape is the result of a complex interplay between the orbiting and infalling terms, an inherently dynamical distinction that cannot easily be made based on the profiles alone (Fukushige & Makino 2001; Diemand & Kuhlen 2008). As a result, conventional fitting functions trained on the orbiting (or one-halo) term struggle to fit simulated or observed profiles in this regime (Becker & Kravtsov 2011; Oguri & Hamana 2011). While some models for the outer profiles have been proposed (Prada et al. 2006; Betancort-Rijo et al. 2006; Tavio et al. 2008; Baltz et al. 2009), they fail to capture the detailed profile shapes (Diemer & Kravtsov 2014, hereafter DK14).

Despite these complications, the transition region and the outer profiles have recently gained renewed relevance because they are much less affected by baryons and because they are sensitive to otherwise inaccessible halo properties. For example, the mass accre-

^{*} Email: diemer@umd.edu

tion rate sets the position of the edge of the orbiting term, which is also known as the splashback radius (DK14, Adhikari et al. 2014; More et al. 2015). Moreover, the outer profiles have become observationally accessible via the density of satellite galaxies and the weak lensing signal around clusters (e.g., More et al. 2016; Baxter et al. 2017; Chang et al. 2018; Shin et al. 2019; Murata et al. 2020; Bianconi et al. 2021). For their inferences, all of these works have relied on the fitting function of DK14, an Einasto profile multiplied by a power-law cut-off term with variable truncation radius, sharpness, and asymptotic slope (a total of 6 free parameters). This flexible function fits averaged profiles to 5–10% accuracy including the transition region, but its design suffered from the same fundamental issue as previous models: at its truncation, the orbiting term is concealed by the infalling term, and its asymptotic shape was thus unknown. As a result, the DK14 fitting function is hard to interpret physically. First, the large number of parameters causes well-known degeneracies that necessitate informative priors (DK14; Baxter et al. 2017; Chang et al. 2018; Umetsu & Diemer 2017). Second, the steepening term approaches a somewhat arbitrary slope that does not actually reflect the shape of the orbiting term. Some observational works have extrapolated this shape based on DK14 fits (e.g. Baxter et al. 2017; Shin et al. 2021), but it is not clear that the results are physically meaningful. Third, the slope of the DK14 profile is a complex function, which makes it difficult to establish the relationship between the profile parameters and physical features such as the splashback radius.

In this paper, we set out to design a more physically motivated fitting function. For the first time, we can draw inspiration from profiles that have been dynamically split into orbiting and infalling particles (using the algorithm presented in Diemer 2022, hereafter Paper I; see also García et al. 2022). Similar splits have recently been explored in observational data using galaxy properties such as colour (Baxter et al. 2017; Adhikari et al. 2021; Shin et al. 2021; O’Donnell et al. 2022; Aung et al. 2022; Dacunha et al. 2022; O’Neil et al. 2022), necessitating a fitting function that captures the shapes of the orbiting and infalling terms. We require that this fitting function should 1) describe the profiles accurately even in the transition region, 2) be flexible enough to apply to individual halos and to stacks with different selection criteria, 3) work across all halo masses, redshifts, cosmologies, and accretion rates, 4) rely on as few free parameters as possible with clear, physical interpretations, and 5) exhibit minimal parameter degeneracies. We achieve these goals with a 5-parameter Einasto-like form with a truncated exponent. Our aim is not necessarily to achieve more accurate fits than DK14 because there are complex variations in the averaged profiles that make it difficult to systematically improve on a 5–10% fit. Moreover, baryons affect the profiles at roughly this level even at large radii (e.g., Veliscig et al. 2014; Schneider et al. 2019). Thus, we instead focus on creating a parameter space that can be used to meaningfully describe observed and simulated profiles. In this second paper of the series, we present and test the fitting function. In Diemer (in preparation; hereafter Paper III), we analyse the resulting parameter space and connect it to halo physics such as accretion histories.

The paper is structured as follows. In Section 2, we mathematically describe previous fitting functions and the new models. We summarize our numerical methods in Section 3, largely referring the reader to Paper I. We assess the quality of our fits to stacked and individual halo profiles in Section 4, and we compare to previously proposed models in Section 5. Section 6 summarizes our results. We discuss an alternative model variant in Appendix B and derive additional mathematical properties in Appendices C and D. Supplementary figures are provided online on the author’s website

at benediktdiemer.com/data. Our fitting function is implemented in the publicly available code COLOSSUS (Diemer 2018).

Throughout the paper, we follow the notation of Paper I. We normalize halo radii by R_{200m} , which encloses an average of 200 times the mean density of the Universe, ρ_m , including all particles (bound or unbound). We denote the mass enclosed within this radius as M_{200m} . We mostly express mass as peak height, $\nu \equiv \delta_c/\sigma(M_{200m})$, where $\delta_c = 1.686$ is the critical density for collapse (Gunn & Gott 1972) and $\sigma(M_{200m})$ is the variance of the linear power spectrum on the Lagrangian scale corresponding to M_{200m} . We define the logarithmic mass accretion rate $\Gamma \equiv \Delta \ln M_{200m}/\Delta \ln a$, measured over one dynamical time (which we define as the mass-independent halo crossing time, about 5 Gyr at $z = 0$). More details on these calculations are given in Paper I.

2 PROFILE MODELS

In this section, we introduce new fitting functions for the orbiting and infalling components of density profiles, which can be combined to fit the entire profile. We describe the general logic of constructing models for the orbiting term in Section 2.1, previously proposed models in Sections 2.2 and 2.3, and our new model in Section 2.4. We introduce a slightly different version of the same model in Appendix B. We also discuss previous and new models for the infalling profile in Sections 2.5 and 2.6. The derivatives of the models with respect to their parameters are given in Appendix C.

2.1 Generalized exponential profiles

Our new function for the orbiting term can be thought of as a generalization of the Einasto profile, where the slope smoothly changes with radius. We write such profiles as the exponential of a radial function $S(r)$,

$$\rho_{\text{orb}} = \rho_s e^{S(r)}. \quad (1)$$

This family of profiles is more intuitively understood by considering the logarithmic slope $\gamma(r)$,

$$\gamma \equiv \frac{d \ln \rho}{d \ln r} = r \frac{dS}{dr}. \quad (2)$$

This expression demonstrates the power of equation (1): we can construct a density profile by defining its logarithmic slope and integrating to get $S(r)$,

$$S(r) = \int \frac{\gamma(r)}{r} dr. \quad (3)$$

Clearly, one condition for the fitting function to be useful is that γ/r must integrate to a reasonably simple, analytical expression. For example, exponential cut-offs in the slope such as $\gamma \propto \exp(r/r_t)$ are problematic because their integrals (if solvable) involve Gamma functions or other complex mathematical expressions.

2.2 The Einasto profile

We begin by reviewing the Einasto profile in light of the discussion above. Its defining feature is a slope of $\gamma = -2(r/r_s)^\alpha$. The parameter α determines how rapidly the profile steepens, and the meaning of the scale radius is that $\gamma(r_s) = -2$. Moreover, the Einasto profile leads to a core at small radii, $\gamma(0) = 0$. The slope integrates to $S(r) = -(2/\alpha)(r/r_s)^\alpha + C$. We can choose to set $C = 0$, in which case ρ_s

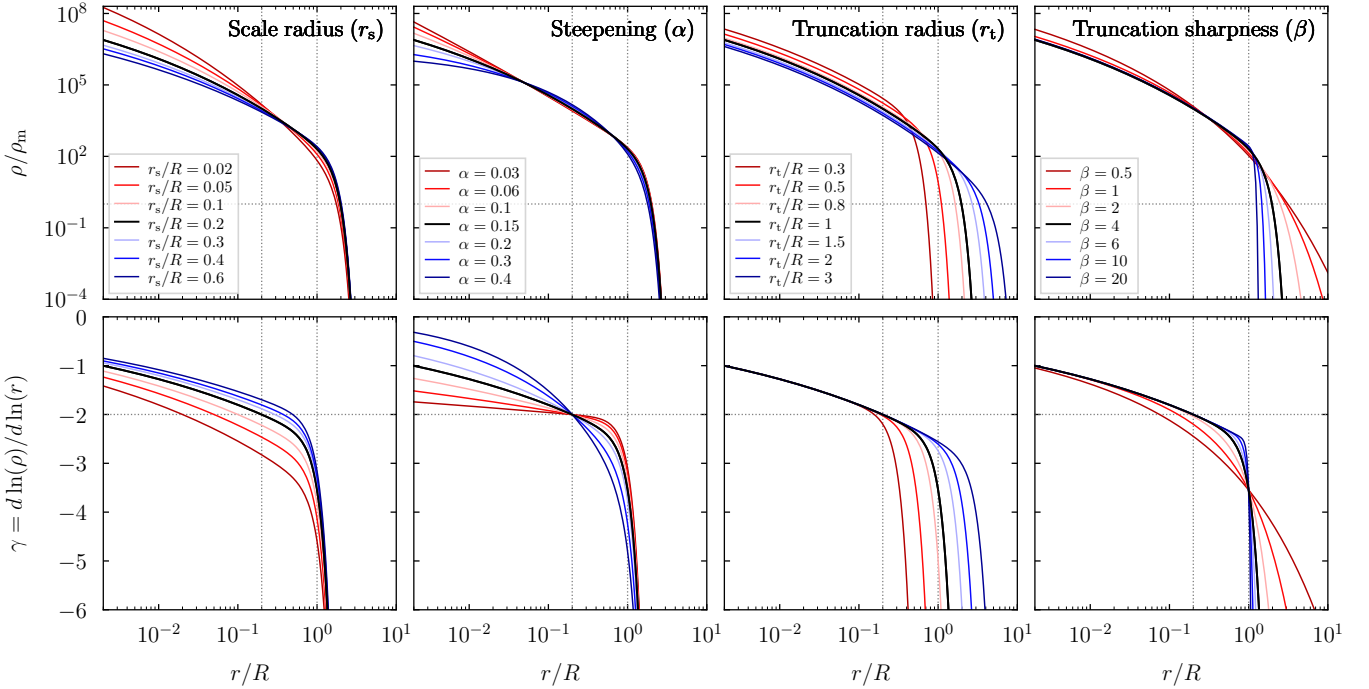


Figure 1. Effect of the free parameters in our model for the orbiting density profile (top) and its logarithmic slope (bottom). Each column shows variations of a single parameter; ρ_s is omitted as it corresponds to a simple normalization. All profiles are normalized by some radius R and integrate to the same $M(R)$. The black lines show the same fiducial profile in each column ($r_s = 0.2 R$, $\alpha = 0.15$, $r_t = R$, $\beta = 4$), and the dotted vertical lines highlight the fiducial r_s and r_t . The horizontal dashed lines mark the mean density in the top panels and a slope of -2 in the bottom panels. All slopes converge to $\gamma(0) = 0$ at the halo centre, but we would need to extend the plot to much smaller radii to see this effect.

describes the density at $r = 0$, but the profile is more commonly written with $C = 2/\alpha$,

$$S(r) = -\frac{2}{\alpha} \left[\left(\frac{r}{r_s} \right)^\alpha - 1 \right], \quad (4)$$

such that $S(r_s) = 0$ and thus $\rho(r_s) = \rho_s$. In practice, we find that the $C \neq 0$ version of the Einasto profile behaves better in least-squares fits because it does not allow a degeneracy between ρ_s , r_s , and α (although the latter two can still be degenerate at fixed ρ_s).

2.3 The DK14 profile

We briefly review the **DK14** model because we will later use its performance as a benchmark for our new model. The model is

$$\rho_{\text{DK14}} = \rho_{\text{Einasto}} \left[1 + \left(\frac{r}{r_t} \right)^\beta \right]^{-\frac{\gamma}{\beta}}, \quad (5)$$

where the steepening term suppresses the density at $r \gtrsim r_t$ as a power law with slope $-\gamma$, while β governs the sharpness of the truncation. Combined with the Einasto parameters, this function has six free parameters, but **DK14** suggested fixing (β, γ) to $(4, 8)$ in fits to mass-selected samples and to $(6, 4)$ when the sample is also selected by mass accretion rate (they did not investigate fits to individual halos). The main disadvantage of equation (5) is that the β and γ parameters do not have a clear physical meaning because the asymptotic slope of the overall orbiting profile depends on r_s , r_t , α , and γ in a complex fashion. Setting β and γ to fixed values reduces the profile to a four-parameter fit with a meaningful truncation radius parameter r_t , but it no longer allows for a varying shape of the truncation term.

2.4 The new model: truncated exponential

In Paper I, we confirmed that the orbiting profile has two characteristic radial scales, which can be captured by the scale and the truncation radii. Moreover, we found that the sharpness of the truncation varies with halo properties and that the profiles decline with an exponential-like, accelerating slope (rather than a constant, power-law slope). Inspired by these observations, we construct a model by adding a truncation term into the slope,

$$\gamma(r) = -2 \left(\frac{r}{r_s} \right)^\alpha - \left(\frac{r}{r_t} \right)^\beta. \quad (6)$$

While similar in spirit, this model significantly differs from the ‘truncated Sersic’ and ‘broken exponential’ models that are popular in the observational literature (e.g. Peng et al. 2010; Erwin 2015). We find the corresponding profile by integrating γ/r ,

$$S(r) = -\frac{2}{\alpha} \left(\frac{r}{r_s} \right)^\alpha - \frac{1}{\beta} \left(\frac{r}{r_t} \right)^\beta + C. \quad (7)$$

For simplicity, we could set $C = 0$, in which case ρ_s would become the density at the centre. A more elegant form is obtained by setting the integration constant such that $\rho(r_s) = \rho_s$,

$$C = \frac{2}{\alpha} + \frac{1}{\beta} \left(\frac{r_s}{r_t} \right)^\beta, \quad (8)$$

and thus

$$S(r) = -\frac{2}{\alpha} \left[\left(\frac{r}{r_s} \right)^\alpha - 1 \right] - \frac{1}{\beta} \left[\left(\frac{r}{r_t} \right)^\beta - \left(\frac{r_s}{r_t} \right)^\beta \right]. \quad (9)$$

We use this parametrisation throughout because the density at r_s is numerically constrained, whereas the central density represents an

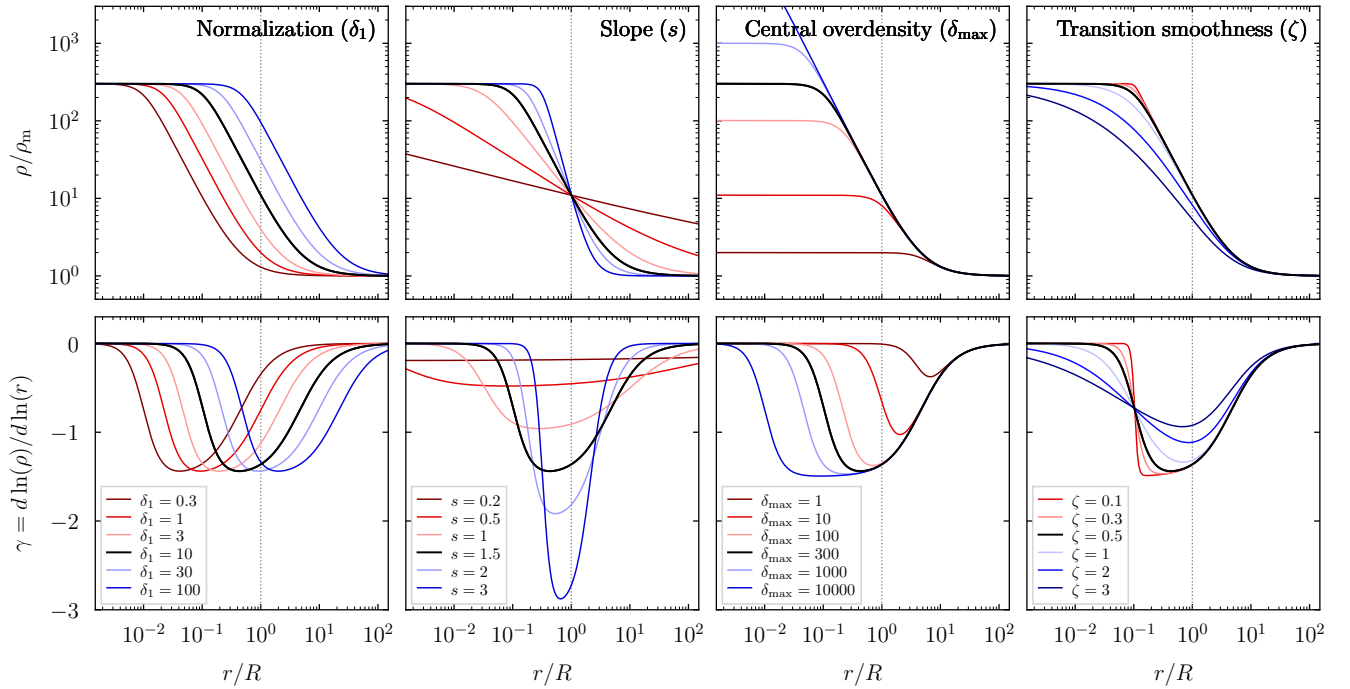


Figure 2. Same as Fig. 1 but for the new infalling profile model, which smoothly transitions from a power law to an asymptotic central density. The parameters are the normalization at radius R , the slope of the power law, the maximum central overdensity, and the transition smoothness. The δ_{\max} parameter can affect the overdensity at R if it is sufficiently small.

extrapolation. However, we give derivatives with respect to the free parameters for both variants in Appendix C2. In Fig. 1, we visually explore how the free parameters affect the shape of our model. Throughout the rest of the paper, we show that equation (9) describes the orbiting profiles with great accuracy.

The model does, however, have two minor shortcomings. First, the truncation term ‘breaks’ the meaning of the scale radius because the slope at r_s is now $\gamma(r_s) = -2 - (r_s/r_t)^\beta$ instead of -2 . The difference is small in most cases since $r_t > r_s$ and generally $\beta \gg 1$, but it can manifest itself for extreme parameter values (red lines in the right two columns of Fig. 1). We note that the $\gamma(r_s) = -2$ condition will likely be violated regardless as soon as an infalling profile is added. Nonetheless, in Appendix B we present a model variant that enforces $\gamma(r_s) = -2$ at the expense of an additional term in $S(r)$. Both models give the same fit and best-fit parameters for virtually all profiles, but the variant can be preferable in cases where r_s and α are strongly degenerate. For either model, the scale radii (and thus concentrations) are directly comparable to those from Einasto fits, but we expect small, systematic shifts similar in scale to the differences between NFW and Einasto concentrations (Dutton & Macciò 2014) or differences due to the fitting procedure (Dooley et al. 2014).

The second shortcoming is that the integrals of ρ , namely the enclosed mass $M(r)$, the projected density $\Sigma(R)$, and the lensing signal $\Delta\Sigma$, cannot be computed analytically. Similar issues hamper even the simpler Einasto profile, where $M(r)$ is a relatively complicated analytical expression (Cardone et al. 2005; Retana-Montenegro et al. 2012) and $\Sigma(R)$ can only be approximated (Dhar & Williams 2010; Dhar 2021). We will investigate similar approximate solutions for the new model in future work, and we have provided fast, numerical solution in the Colossus code (Diemer 2018).

2.5 The infalling profile: previous models

Before shells of dark matter begin to cross, the overdensity due to non-linearly infalling matter is expected to roughly follow a power law with a slope of $-3/2$ (Bertschinger 1985). At large radii, the statistical contribution from large-scale structure comes to dominate, but this transition happens at radii larger than the $10 R_{200m}$ we consider (Paper I). Thus, it is not surprising that DK14 found the profiles to be well-described by a simple power law in overdensity,

$$\rho(r) = \rho_m(z) \left[\delta_1 \left(\frac{r}{R} \right)^{-s} + 1 \right], \quad (10)$$

where δ_1 represents the normalisation at radius R and $-s$ the slope. We will set $R = R_{200m}$ throughout, but any other pivot radius could be chosen instead. One issue with equation (10) is that it can reach arbitrarily high values at small r , which is clearly unphysical. We can prevent this artefact by introducing a maximum overdensity (e.g., Diemer 2018),

$$\rho(r) = \rho_m \left(\delta_1 \left[\frac{\delta_1}{\delta_{\max}} + \left(\frac{r}{R} \right)^s \right]^{-1} + 1 \right). \quad (11)$$

This expression approaches $\rho \rightarrow \rho_m(\delta_{\max} + 1)$ as $r \rightarrow 0$. The exact value of δ_{\max} does not matter because it is reached at radii where the infalling profile dominates by orders of magnitude.

2.6 New infalling model: power law with smooth transition

Inspecting the infalling profiles in Paper I, we found that they do indeed seem to approach a constant density at small radii, but the transition to this value happens less sharply than suggested by equation (11). We thus introduce a transition smoothness parameter, ζ ,

Table 1. Summary of the free parameters of the fitting functions for the orbiting and infalling terms, including their allowed ranges allowed in fits. If the lower and upper bounds are the same, the parameter is held fixed. The last column lists possible modifications in fits to individual profiles. If ‘free’, the same limits apply as for averaged profiles. See Section 2.7 and Appendix A2 for details.

Symbol	Description	Lower	Upper	Ind.
Orbiting term				
ρ_s/ρ_m	Overdensity at scale radius	10	10^7	free
r_s/R_{200m}	Scale radius	0.01	0.45	free
r_t/R_{200m}	Truncation radius	0.5	3	< 10
α	Radial evolution of slope	0.03	0.4	0.18
β	Sharpness of truncation	0.1	10	3
Infalling term				
δ_1	Normalization at R_{200m}	1	100	free
s	Power-law slope	0.01	4	free
δ_{\max}	Central overdensity	10	2000	free
ζ	Smoothness of transition	0.5	0.5	0.5
Model variations				
ρ_0/ρ_m	Overdensity at $r = 0$	10	10^{20}	—
η	Term in Model B (App. B)	0.1	0.1	0.1

$$\rho(r) = \rho_m \left(\delta_1 \left[\left(\frac{\delta_1}{\delta_{\max}} \right)^{\frac{1}{\zeta}} + \left(\frac{r}{R} \right)^{\frac{s}{\zeta}} \right]^{-\zeta} + 1 \right) \equiv \rho_m [\delta_1 Q(r)^{-\zeta} + 1], \quad (12)$$

where we have defined

$$Q(r) \equiv \left(\frac{\delta_1}{\delta_{\max}} \right)^{\frac{1}{\zeta}} + \left(\frac{r}{R} \right)^{\frac{s}{\zeta}}. \quad (13)$$

The shape of this model as a function of its parameters is visualized in Fig. 2. We note that the function’s logarithmic slope,

$$\gamma(r) = - \left(1 - \frac{\rho_m}{\rho(r)} \right) \frac{s}{Q(r)} \left(\frac{r}{R} \right)^{\frac{s}{\zeta}}, \quad (14)$$

remains at a value of $-s$ only across a very narrow radial range for most parameter combinations, if at all. The full freedom of this function allows for very accurate fits, but also for a number of pathological cases where not all parameters are well constrained by the simulated profiles. We find that fixing $\zeta = 0.5$ is a compromise that works for the majority of profiles. The resulting function,

$$\rho(r) = \rho_m \left(\frac{\delta_1}{\sqrt{(\delta_1/\delta_{\max})^2 + (r/R)^{2s}}} + 1 \right), \quad (15)$$

is the infalling profile that we use throughout this paper.

2.7 Allowed ranges of parameters

We impose an allowed range on each parameter to avoid extreme, unphysical values. These flat priors (in logarithmic space) are listed in Table 1. They are designed to be uninformative, with the exception that they enforce $r_s < r_t$. Some parameters are fixed when fitting individual halo profiles (Table 1). We discuss the reasons behind the chosen values in detail in Appendix A2. In Paper III, we will also present the distributions of best-fit parameters for individual and stacked profiles, which could be used as a prior when fitting to observational data. The individual fits can fill out the allowed range of the parameters because not all individual profiles constrain all parameters equally well, whereas the ranges are generous for the averaged profiles.

3 SIMULATIONS AND METHODS

In this section, we describe our simulations and algorithms. In the interest of brevity, we do not excessively duplicate information from Paper I. We briefly summarize our simulations in Section 3.1 and the profile data in Section 3.2, largely referring the reader to Paper I. We devote more detail to our fitting procedure in Section 3.3 and Appendix A.

3.1 N-body Simulations

Our analysis is based on the Erebus suite of dissipationless N -body simulations (Diemer & Kravtsov 2014, 2015), which consists of 14 simulations of 1024^3 dark matter particles (see Table 1 in Paper I). The suite covers different box sizes and resolutions, as well as two Λ CDM and four self-similar cosmologies. The first Λ CDM cosmology is that of the Bolshoi simulation (Klypin et al. 2011), consistent with WMAP7 (Komatsu et al. 2011), namely a flat Λ CDM cosmology with $\Omega_m = 0.27$, $\Omega_b = 0.0469$, $\sigma_8 = 0.82$, and $n_s = 0.95$. The second is a Planck-like cosmology (Planck Collaboration et al. 2014, $\Omega_m = 0.32$, $\Omega_b = 0.0491$, $h = 0.67$, $\sigma_8 = 0.834$, and $n_s = 0.9624$).

We also consider four self-similar Einstein-de Sitter universes with power-law initial spectra of slopes $n = -1, -1.5, -2$, and -2.5 . Here, length and time are scale-free, meaning that the density profiles are independent of redshift when rescaled by a meaningful radius. The self-similar simulations highlight the impact of the initial power spectrum (Efstathiou et al. 1988; Knollmann et al. 2008) and allow us to test a wide range of cosmologies with few simulations because Λ CDM can be seen as an interpolation between different power spectrum slopes. For example, redshift trends in Λ CDM profiles are mostly trends in n (Paper I), meaning that a good fit of our function to profiles from self-similar cosmologies implies a wide range in redshift.

The power spectra for the Λ CDM simulations were generated using CAMB (Lewis et al. 2000). They were translated into initial conditions using 2LPTic (Crocce et al. 2006). All simulations were run with GADGET2 (Springel 2005). We use the phase-space halo finder ROCKSTAR (Behroozi et al. 2013a) to identify haloes and subhaloes. We construct merger trees by connecting halos across time using the CONSISTENT-TREES code (Behroozi et al. 2013b). The resulting halo catalogues are described in detail in Diemer (2020).

3.2 Dynamically split density profiles

The key new ingredient on which we base our models is the splitting of dark matter particles into infalling and orbiting, the transition between which is defined to occur at a particle’s first pericentre (though alternative definitions exist, e.g., Sugiura et al. 2020; García et al. 2022). The pericentres are reliably detected by a novel algorithm that follows the orbit of each particle in each halo. This algorithm was implemented in the SPARTA framework (Diemer 2017, 2020) and applied to all 14 Erebus simulations (Paper I). Despite a few ambiguous particle orbits (e.g., due to the limited time resolution of snapshots), the resulting split profiles were shown to be robust.

We apply the same resolution cuts as in Paper I. We consider only host halos with at least 500 particles within R_{200m} , and we cut out those parts of profiles that lie within $r_{\min} = \max[4\epsilon, 0.133 \Omega_m^{1/3} l(z)]$, where ϵ and $l(z)$ are the comoving force resolution and inter-particle spacing of the simulation. These cuts limit the effects of suppressed centripetal forces and two-body scattering (see Appendix A1 of Paper I for details; Power et al. 2003; Ludlow et al. 2019; Mansfield &

Avestruz 2021). We also impose a limit on the fraction of a halo’s mass that is unbound, $M_{200\text{m,all}}/M_{200\text{m,bnd}} < 1.5$, which excludes halos that are being disrupted by interactions with neighbours (Paper I). However, we find that the effects of neighbours can still significantly distort the mean orbiting profiles of low-mass halos near the truncation. Thus, we exclude profile bins where $\rho < 0.1 \rho_{\text{m}}$ from the fits to mean orbiting profiles, although we do plot those bins in the following figures.

We fit both individual halo profiles and averaged (mean and median) profiles. The latter are constructed by considering halo samples defined by a range of peak height (or mass), a redshift, and possibly mass accretion rate. Each sample combines halos from different Erebus simulation boxes. In the self-similar simulations, there is no physical time, so that each sample combines profiles from different redshifts (Paper I). We calculate a bootstrap uncertainty of the averaged profiles by randomly subsampling them 500 times.

When selecting individual halos, we again apply a lower radial limit of r_{min} (Section 3.2) to avoid poorly resolved parts of the profiles, and we also omit bins that are expected to contain fewer than 5 particles based on the mean profile of the given sample (Paper I). Additionally, we only fit well-resolved halos with $N_{200\text{m}} \geq 5000$ because their larger resolved radial range leads to less noisy distributions of the best-fit parameters. In total, we have fitted the profiles of about 378 000 halos in the WMAP7, Planck, and self-similar cosmologies. The WMAP7 sample shrinks with redshift from about 45 000 at $z = 0$ to about 1300 at $z = 6$. Similarly, the self-similar samples shrink from about 120 000 halos in the $n = -1$ simulation to about 13 000 in the $n = -2.5$ box.

3.3 Fitting procedure

Fitting density profiles is notoriously fickle, and the chosen routine can systematically influence the results (e.g., O’Neil et al. 2021). We have designed a robust routine, which we describe in detail in Appendix A1. We minimize the logarithmic residual between data and fitting functions using a Cauchy loss function, which severely reduces influence of outliers. For averaged profiles, the residual is compared to the bootstrap error plus a 5% systematic uncertainty added to all bins. For individual halos, we use the sum of the Poisson error due to (potentially) low number of particles and an arbitrary 25% systematic error. Each fit is performed multiple times from a number of initial guesses to ensure that the true minimum is found (see Appendix A1 for details).

4 RESULTS

In Sections 4.1 and 4.2, we fit averaged and individual profiles, respectively, and analyse the quality of the fits. Given the large parameter space of mass, redshift, cosmology, and accretion rate, we show only representative examples and refer the reader to a collection of additional online figures (Section 1).

4.1 Fits to averaged profiles

Figs. 3 and 4 show median and mean profiles for a wide variety of halo samples. We omit intermediate bins to avoid crowding the figures; their profiles fall between those shown. As in Paper I, all profile plots are split into total, orbiting, and infalling profiles (from top to bottom), with smaller panels showing the logarithmic slope and the fractional deviation of the fitting function from the profiles. We show the latter on a symmetric log scale, with the region between

$\pm 5\%$ being linear. The dotted lines highlight differences of 5%, 10%, and 20% to guide the eye.

In this section, we focus on fits with the full parameter freedom, that is five parameters for the orbiting term (Section 2.4) and three for the infalling term (Section 2.6). The orbiting and infalling profiles are fit separately with the respective models, and the results serve as initial conditions for a combined fit to the total profiles (in which we vary all parameters except for δ_{max} ; Section 2.7). Thus, the total fits differ from the sum of the orbiting and infalling fits. In Paper III, we will calibrate some parameters to produce a more predictive profile model.

4.1.1 The total profile

We begin by evaluating fits to the median and mean total profiles, shown in the top rows of Figs. 3 and 4. These fits do not make use of the separate orbiting and infalling components. In the left columns, we split halo samples from the WMAP7 cosmology by mass, or rather by peak height, ν . The corresponding mass bins range from $M_{200\text{m}} \approx 1.4 \times 10^{10} M_{\odot}$ ($\nu = 0.5$) to $M_{200\text{m}} > 8 \times 10^{14} M_{\odot}$ ($\nu > 3$). In the second column we investigate the redshift evolution of the $2 < \nu < 3$ bin, which corresponds to $1.4 \times 10^{14} < M_{200\text{m}}/M_{\odot} < 8 \times 10^{14}$ at $z = 0$ and to $7 \times 10^8 < M_{200\text{m}}/M_{\odot} < 4.2 \times 10^{10}$ at $z = 6$. The total profiles are fit excellently, to within 5% or better. The slope panels demonstrate that the fits faithfully reproduce the complicated shape evolution of the profiles. Moreover, we do not notice any significant differences in the fit quality to the median and mean total profiles. The results are essentially the same for the Planck cosmology or for other bins in peak height.

DK14 and Paper I showed that the profile shapes depend more fundamentally on the mass accretion rate, Γ , than on mass, redshift, or cosmology. Many of the apparent trends with mass are actually trends in Γ , which are convolved with the mass-dependent distribution of accretion rates (larger halos accrete more actively when structure forms hierarchically). In the third columns of Figs. 3 and 4, we split the $2 < \nu < 3$ bin by accretion rates; the trends are the same for other peak heights (Paper I). An accretion rate of $\Gamma \lesssim 0.5$ corresponds to pure pseudo-evolution due to the evolving overdensity threshold (Diemer et al. 2013), meaning that the sample shown in black has undergone essentially no actual changes to the density profile over the past dynamical time. Conversely, halos with $\Gamma > 4$ (yellow) have grown rapidly. Fitting the resulting profiles is more challenging than for mass-selected samples because they exhibit a greater diversity of shapes. Nonetheless, our model fits the Γ -selected profiles almost as well as their ν -selected counterparts, namely to about 5% within the statistical uncertainties in most samples and to about 10% for the most extreme (low or high) accretion rates. One exception are the ‘wiggles’ near the second caustic in low- Γ profiles, where the fit can deviate by up to 20%. These caustics form at the second orbit of recently accreted particles (Adhikari et al. 2014), but modelling this feature in our function would introduce significant complexity for a modest return in accuracy.

Finally, the right columns of Figs. 3 and 4 show profiles from the self-similar simulations. We have selected halos by both ν and Γ to isolate the effect of the slope of the linear power spectrum, n . Even though extreme values such as $n = -1$ lead to profiles that differ significantly from Λ CDM, the total profiles are fit to 5% or better (subject to the trends with Γ discussed above). This match gives us confidence that our model can fit profiles in a wide range of cosmologies.

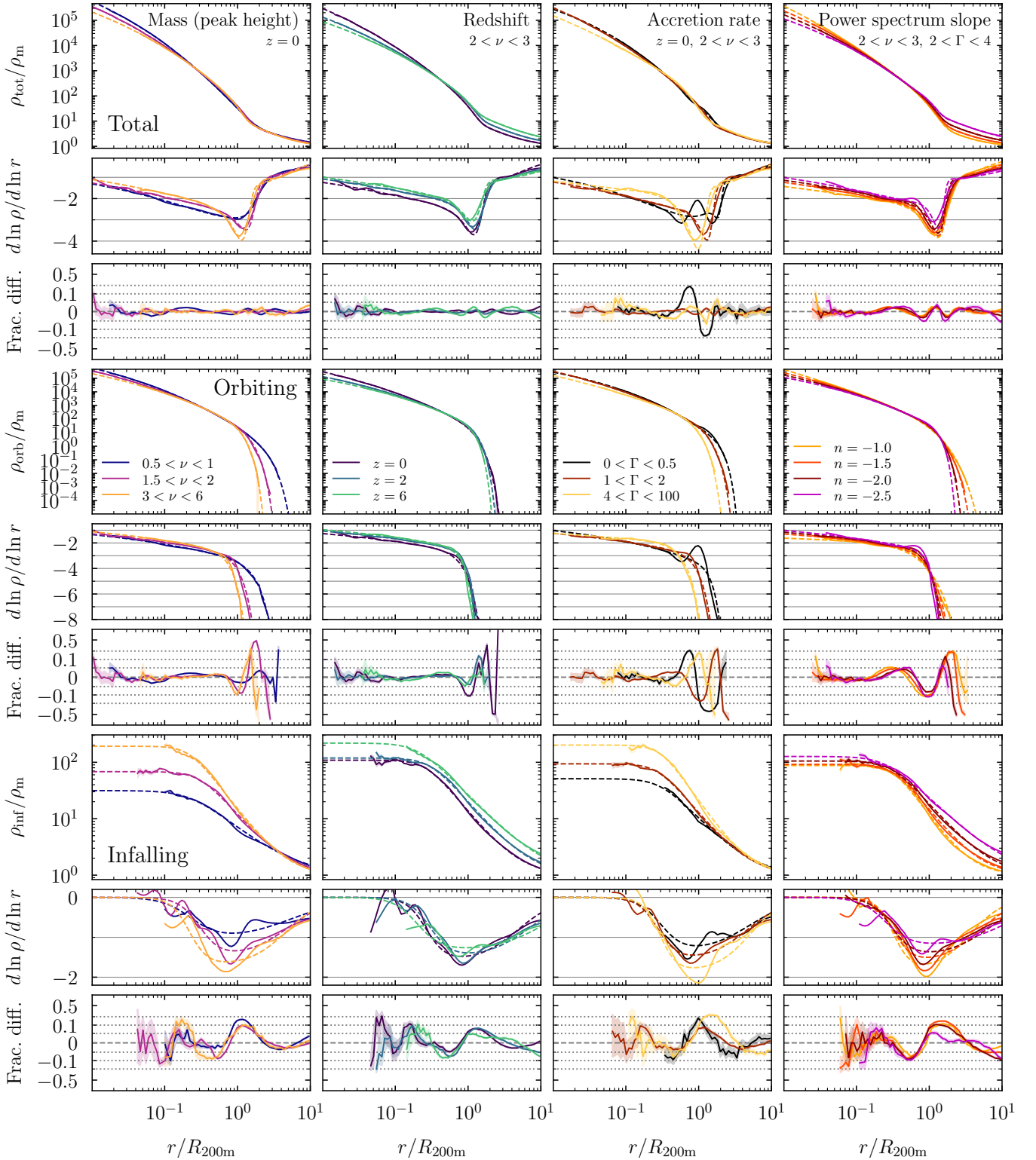


Figure 3. Fits to the selected median profiles of halos binned by mass, redshift, accretion rate, and power spectrum slope (from left to right). Large panels show the total, orbiting, and infalling profiles (solid lines, from top to bottom), as well as fits (dashed lines). The smaller bottom panels show the logarithmic slope and the relative difference between simulation and fit, plotted on a symmetric log-scale where the range between $\pm 5\%$ is linear; the dotted gray lines mark 5%, 10%, and 20%. Shaded areas highlight the statistical uncertainty. The first column shows mass-selected samples in the WMAP7 cosmology. The second column shows the redshift evolution of a representative peak height bin ($2 < \nu < 3$). In the third column, this bin is additionally split by accretion rate. The fourth column compares profiles at fixed ν and Γ in self-similar cosmologies. The total profiles are fit to 5% accuracy, with the only exception of the wiggles in low- Γ profiles that are caused by particles on their second orbit. The orbiting profiles are fit to $\sim 10\%$ except where they sharply drop and even tiny differences in density lead to large relative differences. The infalling profiles are similarly fit to between 10% and 20% accuracy, depending on the halo sample.

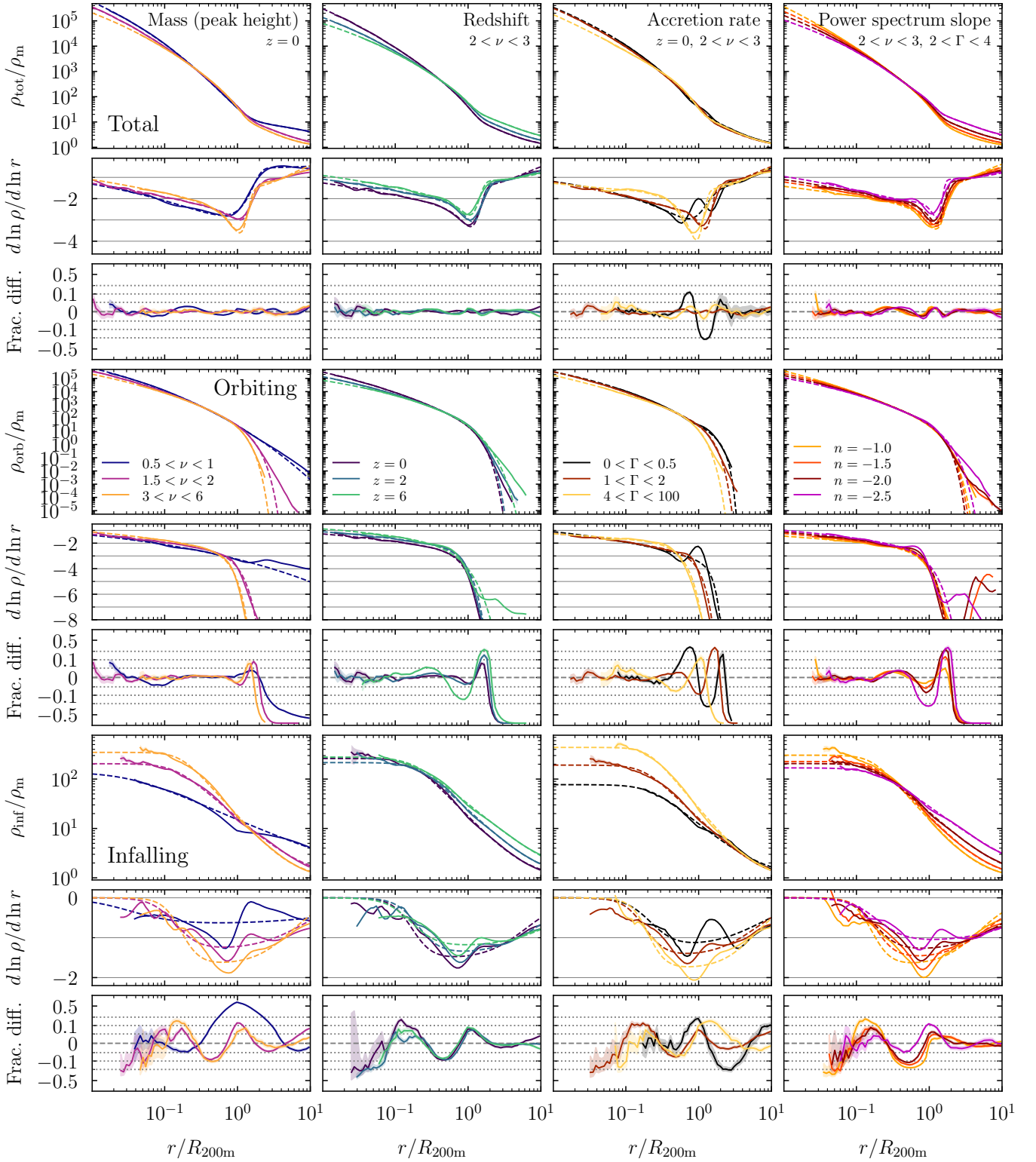


Figure 4. Same as Fig. 3 but for mean rather than median profiles. The total mean profiles are fit as well as their median counterparts. Similarly, the mean orbiting profiles are fit to about 10% accuracy except at the truncation. The fit ignores bins where the density falls below $\rho = 0.1 \rho_m$; the corresponding deviations are driven by the influence of neighbouring halos and thus not particularly meaningful. The mean infalling profiles are fit less accurately than the medians, largely because they show strong effects of the R_{200m} boundary that is used to define subhalos. However, this issue has no impact on the total profiles.

4.1.2 The orbiting term

We now turn to the orbiting profiles (rows 4–6 in Figs. 3 and 4). The exact quality of the fit is somewhat academic because the orbiting and infalling terms cannot be exactly distinguished in observations, but it was a stated goal for our model to capture the physical nature of the orbiting term. At its truncation, however, the orbiting term becomes slightly sensitive to the numerical definition of particles' pericentres (Paper I). Moreover, particles can be tidally stripped by interactions with nearby neighbours. While we try to suppress this effect by excluding halos with a large unbound component (Section 3.2), a few 'orbiting' particles can be dragged to arbitrarily large radii. Given that this artefact is caused by relatively few halos, the resulting differences are much more apparent in the mean than in the median profiles. These issues caution us not to over-interpret fitting errors at very low densities, which can reach $\rho = 10^{-5} \rho_m$ in some mean profiles. We thus ignore densities below $\rho < 0.1 \rho_m$ in fits to the mean orbiting profiles.

The ν -selected orbiting profiles are fit to 10% accuracy out to roughly the truncation radius, where the relative differences can become arbitrarily large. As for the total profiles, we find a somewhat degraded fit quality in Γ -selected samples, chiefly because the second-caustic wiggles are more pronounced in the orbiting than in the total profiles where the infalling term partially smooths them out. Overall, the fit quality is a little better for the median profiles than for the means.

4.1.3 The infalling term

Fitting the infalling term to small radii is an entirely new challenge because the shape of this contribution at $r \lesssim 0.5 R_{200m}$ was hitherto concealed by the orbiting component. Key insights from Paper I were that the infalling term approaches a constant value at small radii, continuously steepens with radius towards the truncation radius, and flattens again beyond r_t . However, the detailed profile shapes are diverse and depend on ν , Γ , and n , as evidenced by rows 7–9 of Figs. 3 and 4.

Our model fits most median infalling profiles to about 10% and some Γ -selected samples to 20% accuracy, with no real trend with redshift, mass, or cosmology. Some of the deviations seen at small radii are not statistically significant considering the uncertainties (shaded areas). The mean infalling profiles are more difficult to fit and can deviate by more than 20% for low-mass samples. One reason is that the mean profiles are noticeably affected by nearby neighbours, and thus by the definition of subhalos as residing within R_{200m} (Paper I). This arbitrary boundary leads to sharp features around R_{200m} (e.g., blue lines in the left column of Fig. 4), which cannot (and should not) be fit by our simple power-law expression.

4.1.4 Summary

We find that the new truncated-exponential model provides 5–10% fits to the total mean and median profiles selected by mass and/or accretion rate. Any features that are systemically fit poorly are understood to be somewhat unphysical (e.g., due to neighbouring halos), too detailed for a fitting model (second caustic), or susceptible to noise (the exact shape at the orbiting truncation, where the density plummets to very low values). We note that baryonic effects enter at about the same level of accuracy, meaning that a more accurate fit would need to rely on hydrodynamical simulations. Fitting the orbiting and infalling terms separately poses a greater challenge, but the fitting function still captures their salient features and provides

good accuracy over the radial ranges where the profiles are well-constrained.

We have also experimented with fitting the averaged profiles of subhaloes. Here, we select by bound (as opposed to total) mass. The SPARTA algorithm keeps identifying first pericentres after a halo becomes a subhalo, but the orbiting term will increasingly include host material that the subhalo has drifted through. When binning by the resulting peak height, the truncated exponential model fits the median orbiting profiles reasonably well, as they do exhibit a clear truncation. The mean profiles, however, appear fairly irregular due to some subhaloes with strong host contributions. Similarly, the 'infalling' term now contains mostly host material and follows an entirely different shape from that of host haloes. Given these difficulties, we leave an investigation of subhalo profiles to future work.

4.2 Fits to individual halos

One requirement for our fitting function was that it should fit the total profiles of individual halos, as well as their dynamically split components. For each halo in our sample of 378 000, we separately fit equation (9) to the orbiting term (fixing $\alpha = 0.18$ and $\beta = 3$) and equation (15) to the infalling term (Section 3.3). We then use the best-fit parameters as the initial guess in a combined fit to the total profile. As discussed previously, individual halo profiles generally do not contain sufficient information to simultaneously constrain r_s and α , or to reliably determine r_t (necessitating other ways to measure the splashback radius, such as the SPARTA algorithm). Thus we experiment with different levels of parameter freedom in the combined profiles. In one case, we let all parameters except δ_{\max} float. This procedure naturally leads to the best fit in a statistical sense, but we observe numerous degeneracies and unphysical behaviour where the infalling profile adjusts to make up for a poor fit to the orbiting term. To avoid these issues, we also run fits where we vary only ρ_s and r_s in the combined fit, meaning that r_t , δ_1 , δ_{\max} , and s are fixed to their values from the separate fits. Given the restricted freedom of the combined fits, they are generally very similar to the sum of the separate fits. The goal of the restricted fits is not to find the formally most optimal fit but to obtain meaningful best-fit parameters. We compare the fit quality of both types of fit to the NFW and Einasto models in Section 5.2. In Paper III we show that the totally free fits do recover the parameters of the separate orbiting and infalling fits on average, albeit with large scatter.

Fig. 5 shows a few representative example fits. Each panel shows the orbiting, infalling, and total profiles of an individual halo as solid lines; the logarithmic slopes are omitted because they are noisy for individual halos. Our model (dashed lines) fits the profiles well within statistical error and stochastic variations, except for the bottom-right panel which was selected to show a poor fit. The top row shows halos with increasing accretion rates. As discussed in Paper I, their peak height (mass) has very little influence on the profile shapes, but the increasing Γ clearly manifests itself in decreasing values of r_t/R_{200m} and a sharper truncation. The second row of Fig. 5 shows a number of examples from other redshifts and cosmologies. First, at high redshift, the average mass accretion rate is higher, which can lead to very small truncation radii such as in the left bottom panel, where r_t reaches the minimum imposed in our fits, $0.55 R_{200m}$. However, we have not observed examples where the true r_t is so much smaller than this limit that it would lead to a bad fit. The high accretion rate also leads to a prominent infalling profile, with $\delta_1 \approx 45$ at R_{200m} ; this example shows that our generous upper limit of 100 is necessary. The second and third panels demonstrate that our functions for the orbiting and infalling profiles can

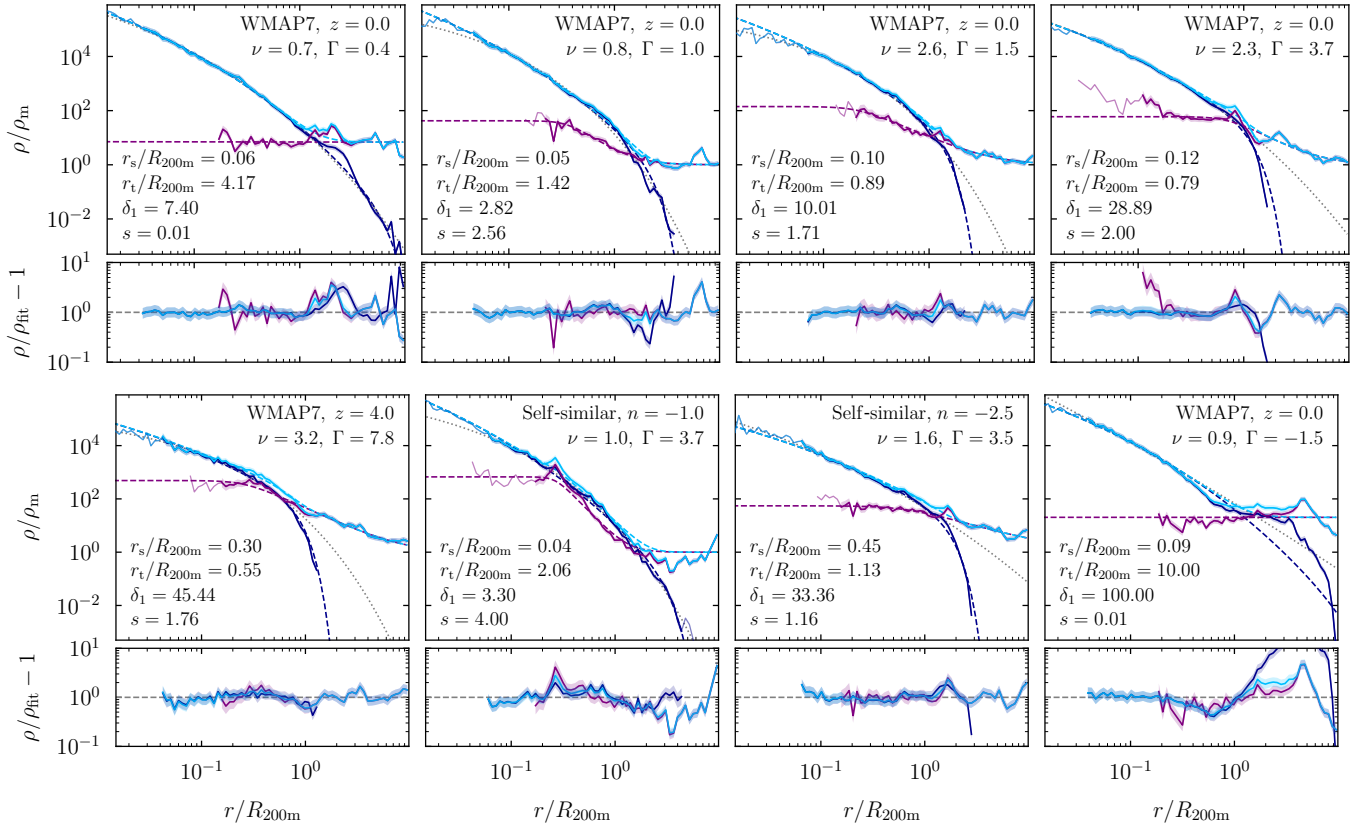


Figure 5. Representative examples of fits to individual halo profiles. Solid lines show the orbiting, infalling, and total profiles (in dark-blue, purple, and light-blue, respectively). Shaded contours highlight the combination of statistical and systematic error that is used in the fits (equation A3). Thin lines without error contours indicate unreliable profile bins smaller than the resolution limit. The dashed dark-blue and purple lines show fits of our models for the orbiting and infalling terms; the dashed light-blue lines correspond to the sum of these fits rather than the combined fit. The dotted gray lines show a three-parameter Einasto fit to the orbiting term for comparison. The legends in each panel list properties of the halo in question and the most informative best-fit parameters. The top row shows halos from the WMAP7 cosmology at $z = 0$ with ascending Γ , which leads to a decreasing r_t/R_{200m} . The normalization, slope, and asymptotic values of the infalling profiles differ dramatically between individual halos. The bottom row shows a few extreme cases. First, a halo at $z = 4$ has a very high accretion rate, $\Gamma \approx 8$, which leads to a truncation radius at the lower limit of $r_t \geq 0.55 R_{200m}$ as well as a high normalization of the infalling profile. The second example is a halo in the $n = -1$ self-similar cosmology, which often produces very steep infalling profiles that can reach our maximum of $s = 4$. Conversely, the $n = -2.5$ cosmology commonly produces shallow, power-law like total and infalling profiles with low concentrations (third example). The final example was deliberately picked to represent a poor fit, in this case because of a large amount of orbiting material at large radii. While an Einasto profile with the same number of free parameters (α instead of r_t) can fit low- Γ profiles, it cannot capture the sharp truncation (dotted lines).

fit extreme cases, which are often found in the self-similar simulations with very different power spectrum slopes. For example, the infalling profile in the second panel reaches the maximum slope of $s = 4$, and infalling matter contributes equally to orbiting matter all the way to $r \approx 0.2 R_{200m}$. Conversely, the third panel shows a halo with flat infalling and orbiting profiles, which lead to r_s reaching the maximum of $0.45 R_{200m}$. Finally, the bottom right panel was selected to show a poor fit, in this case because of a major merger that deposited unusually large amount of orbiting material at large radii.

We conclude that the new truncated-exponential model captures individual profiles well, including the full range of halo properties and cosmologies investigated. In Section 5.2, we furthermore show that the model outperforms the Einasto function without a truncation. In Paper III, we analyse the resulting parameter distributions in detail.

5 COMPARISON TO OTHER MODELS

We have convinced ourselves that the new fitting function successfully reproduces simulated profiles, but we should also ask how

unique that success is and whether it could be achieved with fewer free parameters. In Section 5.1, we compare models for the orbiting term based on averaged profiles, where we can discern the detailed shapes that lead to the success or failure of certain fitting functions. In Section 5.2, we evaluate the fit quality for individual halos by comparing to the NFW and Einasto forms. In Section 5.3, we compare the surface density profiles and lensing signal to other models and show that the features of the three-dimensional profiles do persist in projection. In Section 5.4, we consider models based on the distribution function and discuss the dynamical properties of the new model.

5.1 Models for the orbiting term

Fig. 6 shows a comparison of different fits to the total and orbiting profiles of two representative halo samples. The infalling part of the total profile is fit with equation (15) in all cases and is thus omitted from the figure. The slope panels for the orbiting term reach down to extremely steep slopes to highlight the predictions for the asymptotic

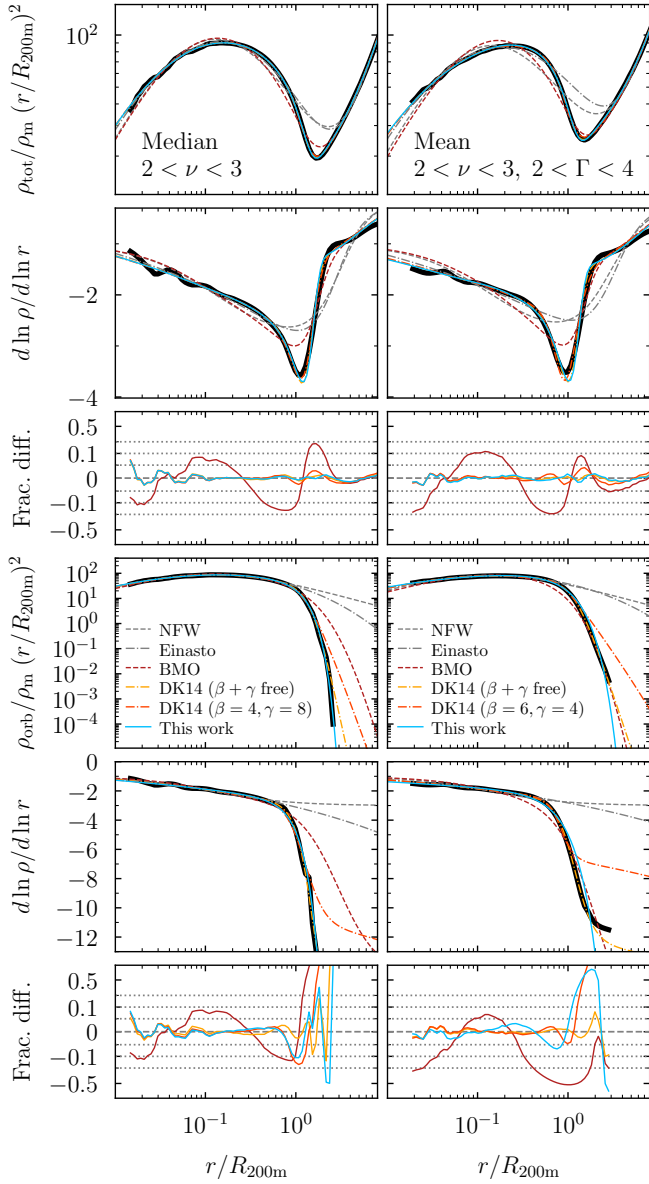


Figure 6. Comparison of different fitting functions for the orbiting term. The profiles in rows 1 and 4 are rescaled by r^2 to compress the dynamical range. The following rows show the logarithmic slope and fractional differences, as in Figs. 3 and 4. The columns show two representative orbiting profiles (thick black lines), namely the median profiles of halos with $2 < \nu < 3$ (left) and the mean profiles of a sub-sample additionally selected to have $2 < \Gamma < 4$ (right). The statistical uncertainty on the average profiles is smaller than the thickness of the black lines. The gray lines show NFW (dashed) and Einasto (dot-dashed) profiles, which are not designed to fit the sharp truncation of the orbiting term; those profiles are omitted from the difference panels for clarity. The coloured lines show the profiles of Baltz et al. (2009, BMO, dashed maroon), DK14 with the slopes β and γ as free parameters (yellow dot-dashed), DK14 with the slopes fixed to their suggested values for ν - and Γ -selected samples (orange dot-dashed), and the new model (light blue). While the full-freedom DK14 fits well, it has an extra free parameter compared to the new function. Moreover, it is clear that its slope asymptotically approaches a certain log-linear evolution with radius due to the underlying Einasto profile. This shape fundamentally differs from the observed truncation, which is reproduced by the new model. For this figure we fit to the entire radial range of the mean profiles, including possibly unphysical features at low density that are over-fit by the free DK14 model (right column).

shape of this component that are made by different fitting functions (without the benefit of knowing the split profiles, of course).

Most previously proposed fitting functions encounter at least one of two fundamental issues. First, Paper I showed that the slope of the orbiting term reaches arbitrarily steep values (as low as -13 in Fig. 6). This kind of cut-off cannot be captured by power laws because they inevitably asymptote to a fixed slope at large radii. For example, the NFW profile approaches a slope of -3 (dashed gray lines), too shallow for the simulated profiles at $r \gtrsim r_t$. This issue persists for profiles with other slope transitions such as Burkert (1995) or superNFW (Lilley et al. 2018), models with steeper outer slopes (Hernquist 1990), or even more complicated combinations of power-law slopes such as generalized power-law models (Zhao 1996; An & Zhao 2013; Di Cintio et al. 2014; Dekel et al. 2017; Freundlich et al. 2020). To improve the fit of NFW profiles around the transition region, Baltz et al. (2009, BMO) introduced a multiplicative steepening, $\rho \propto \rho_{\text{NFW}} \times [r_t^2 / (r^2 + r_t^2)]^n$ (maroon dashed lines in Fig. 6). This form can fit the total profiles to about 25% accuracy, but it fails to capture the orbiting term because it approaches a fixed slope of $-3 - 2n$. Here $n \approx 11$, a value much larger than the $n \approx 2$ usually employed to fit weak lensing signals (Oguri & Hamana 2011). An approach similar to BMO was taken by Tavio et al. (2008); we do not include their function in Fig. 6 because it was already shown not to reach sufficiently steep slopes (fig. 15 in DK14).

The second fundamental problem encountered by many fitting functions is that the orbiting profiles have two physical scales, which can be expressed as r_s and r_t . These scales are set by different epochs in a halo’s accretion history, namely, by the formation time, which correlates with c , and r_t , which correlates with the recent accretion history (Wechsler et al. 2002; Tasitsiomi et al. 2004; Zhao et al. 2009; Ludlow et al. 2013; Lucie-Smith et al. 2022b; Shin & Diemer 2022). The need for an extra variable to describe the profiles can be independently discovered using machine learning (Lucie-Smith et al. 2022a). Single-scale functions cannot address this problem and typically smooth over the sharp truncation, though they may work if the fit does not extend beyond roughly R_{vir} . The Einasto model exemplifies this behaviour: while its slope can reach arbitrarily steep values in principle, the steepening occurs at the same pace at all radii (gray dot-dashed lines in Fig. 6). Some models have introduced a second radial scale to account for variations at small scales, e.g., in the coreNFW (Read et al. 2016) or coreEinasto (Lazar et al. 2020) models, but these modifications obviously do not change the fit at large radii. Springel & White (1999) suggested $\rho \propto \exp[-(r - R_{200c})/r_s]$ to model tidal truncation, but this term does not introduce a new scale and thus cannot capture variations in r_t/r_s (see also Fielder et al. 2020).

To account for the second radial scale and the strong steepening, DK14 introduced a flexible truncation term (Section 2.3). Their results were based on the same simulations as this paper, but they did not split profiles into orbiting and infalling, meaning that their functional form (equation 5) cannot be expected to reproduce the truncation shape at low densities. Fig. 6 shows two versions of the DK14 model. In the first, the sharpness of the transition, β , and the asymptotic slope of the steepening term, γ , are free parameters (hereafter ‘DK14-6’, yellow dot-dashed lines). In the second, they are fixed to the optimal values recommended by DK14, namely $\beta = 4$ and $\gamma = 8$ for the ν -selected sample in the left column and $\beta = 6$ and $\gamma = 4$ for the Γ -selected sample on the right (hereafter ‘DK14-4’, orange dot-dashed lines). We will keep in mind that the former version has one more free parameter than the new model, and the latter one fewer.

Fig. 6 demonstrates that the DK14 profile approaches unphysical slopes at large radii: regardless of the power-law slope γ , the expo-

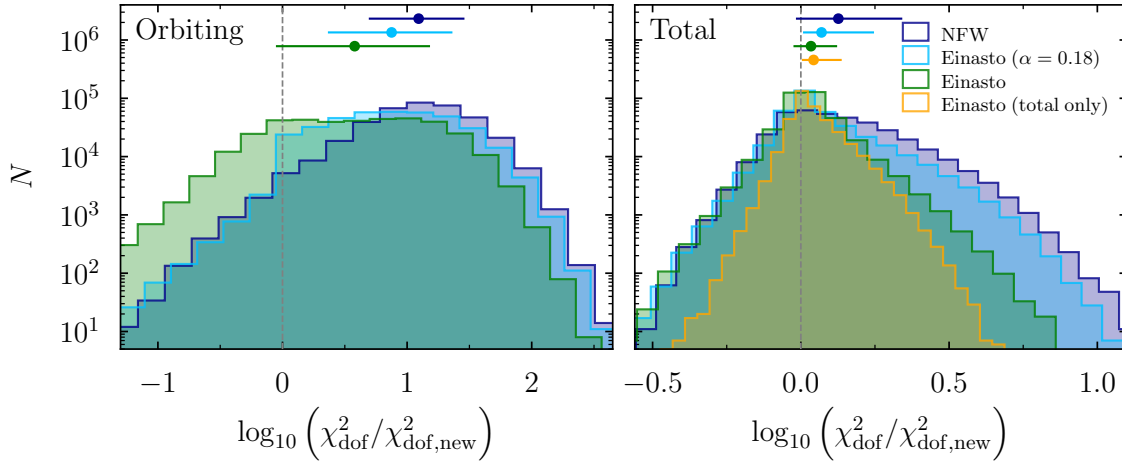


Figure 7. Comparison of the relative fit quality of equation (9) and the NFW and Einasto models, for all 378 000 halos in our individual halo sample. The functions have been applied to the orbiting term (left) and to the total profile (right). All models including the same fit to the infalling profile. The histograms show the logarithmic ratio of χ^2/N_{dof} between each model and our new model (with three free parameters, ρ_s , r_s , and r_t). The points with error bars mark the mean ratio and 68% interval (the median ratios are very similar). When fitting the orbiting term, the new model strongly outperforms the three-parameter Einasto profile (green), highlighting that freedom in α is not sufficient to fit the truncation. When fitting the total profiles but keeping α and r_t fixed based on the separate fit (right panel), the fit quality is improved by 10% on average (and a median of 5%). This result holds even when fitting only to the total term with no knowledge of the split profiles (yellow). Fixing α in the Einasto fits (light blue) degrades the orbiting fit but also reduces the number of degrees of freedom so that the χ^2/N_{dof} difference in the total fits remains similar. The two-parameter NFW model compares less well than the Einasto profile (dark blue).

nential term from the Einasto profile eventually takes over and leads to a gradually steepening slope that does not match the simulated profiles. While this transition occurs at steep slopes (e.g., about -10 in the left column of Fig. 6) and does not cause noticeable fit errors, it does lead to a conceptually wrong prediction for the shape of the orbiting term. For the purposes of this test, we have included even radii with low mean densities in the fit (unlike in our fiducial procedure, see Section 3.2).

We can get a quantitative sense of the new and DK14 fits by comparing their χ^2/N_{dof} values. The conclusions depend somewhat on whether samples are selected by ν only or also Γ , mean and median, and whether we consider the DK14-6 or DK14-4 variants. We first consider fits to only the orbiting term, which test whether the fitting function physically describe the correct underlying profile. As expected, the new form outperforms DK14-4 for virtually all mean and median samples, and often by a sizeable margin, with $\Delta_\chi \equiv \Delta \log_{10}(\chi^2/N_{\text{dof}})$ of up to 2. Compared to the DK14-6 form that has one more free parameter, the median ν -selected profiles tend to be better fit by the new form, and the mean profiles by DK14-6. Most Γ -selected samples are better fit by DK14-6, but at the expense of an extreme range of best-fit β and γ . The new model better fits particularly sharp truncations in median samples with $\Gamma \gtrsim 2$. All differences in fit quality are strongly reduced when fitting the total rather than the orbiting profiles, but DK14-4 still tends to perform slightly worse and DK14-6 slightly better and in most fits. Some of the latter model’s success, however, arises from overfitting profiles that carry signatures of neighbouring halos, which leave a power-law tail that the DK14 fit latches onto. Physically, it is not clear that the profile model should fit such profiles.

In summary, we confirm the expected trend that models with more free parameters achieve a lower χ^2/N_{dof} . However, giving the DK14 model its full freedom of 6 parameters often leads to meaningless values of β and γ . Our new truncated-exponential model achieves more physical asymptotic profiles and a comparable fit quality with fewer, well-defined parameters.

5.2 Individual profiles

While the examples of individual halos in Fig. 5 are encouraging, we need a quantitative metric to decide whether the additional complexity of the new model is warranted compared to simpler functions. Without an absolute measure of fit quality in the absence of a well-motivated uncertainty on the profiles (Appendix A1), our best option is to compare the relative χ^2/N_{dof} of different fits. To this end, we repeat the procedure described in Section 4.2 with three models: NFW, Einasto with free α , and Einasto with $\alpha = 0.18$. In Fig. 7 we compare these fits for all 378 000 halos in our individual sample. While there are mild trends when we break up the sample by cosmology and redshift, the overall picture remains unchanged.

The most ‘fair’ comparison is between the new model and an Einasto profile with free α because both have three parameters. When fitting only the orbiting profile, the new model has a lower χ^2/N_{dof} by a median factor of four (green histogram in the left panel of Fig. 7). This dramatic improvement highlights that the truncation cannot generally be fit with Einasto profiles. This observation is also apparent in Fig. 5, where low- Γ halos are well described by the Einasto form (gray dotted lines) but where the increasingly sharp truncation leads to poor fits at large radii.

In realistic applications, however, we fit to total profiles. This case is shown in the right panel of Fig. 7. We test two variations of the fits. First we vary only ρ_s and r_s in the combined fit, keeping α , r_t , and the parameters of the infalling profile to their values from the separate fits (green). The new model now improves χ^2/N_{dof} by about 10% on average because exact shape of the truncation is less important in total profiles. Moreover, in most real-world applications, we do not have access to the separate orbiting profile. This result holds when we ignore the results of the separate orbiting fit and let all free parameters of the orbiting term vary (yellow). This relatively modest difference reminds us that it is difficult to extract the truncation radius from total individual profiles, but it still represents a measurable improvement over the Einasto model. We also compare the new model to the two-parameter Einasto fit with $\alpha = 0.18$ and

to the NFW profile (light and dark blue histograms in Fig. 7). The orbiting profile is described much less accurately by these forms, with mean χ^2/N_{dof} increases of about 7 and 12, respectively. Once again, the difference is much smaller when fitting the entire profile, with mean increases of 17% and 34%. We have confirmed that these results remain unchanged when directly optimizing χ^2 instead of the Cauchy loss function $\ln(1 + \chi^2)$ (Appendix A1).

Overall, Fig. 7 provides strong justification for our new fitting function because it improves the fit quality at a fixed number of free parameters. While this improvement is most noticeable when fitting the orbiting term separately, we also record a statistically significant improvement when fitting the total profiles without any knowledge of the orbiting term. We conclude that the new function captures both averaged and individual profiles well. In Paper III, we analyse the connection between the properties of individual halos and their best-fit parameters.

5.3 Projected profiles and lensing signal

While we have demonstrated that the new profile model is preferred by simulated halo profiles, the three-dimensional density profile is generally not accessible in observations. In general, we measure either the surface density or the lensing signal. The surface (or projected) density, $\Sigma(r)$, can be measured via the satellite distribution, for example (More et al. 2016). The lensing signal corresponds to the excess surface mass density, $\Delta\Sigma \equiv \bar{\Sigma}(< r) - \Sigma(r)$, the difference between the averaged surface density within a given radius and the surface density at that radius. In this section, we investigate how different the new profile is from other models in projection, and whether variations in the truncation radius can, in principle, be extracted from observational data.

In Fig. 8, we show projected profile quantities for a typical cluster halo with $M_{200\text{m}} = 5 \times 10^{14} h^{-1} M_{\odot}$ and $c_{200\text{m}} = 5$ at $z = 0$. We set $\alpha = 0.18$ and $\beta = 0.3$, but we vary r_t between values corresponding to low and high accretion rates (about $0.7 < r_t/R_{200\text{m}} < 1.2$, Paper III). The surface density profiles of these models can easily be distinguished by eye, and all truncated exponential profiles visibly differ from the NFW and Einasto forms. The differences are smaller in the lensing signal, but they persist across a wide radial range. This finding highlights that the entire profile must be fitted in order to extract the full information content (e.g., Khakaj et al. 2020, 2022).

5.4 Dynamical models

Assuming that halos are in dynamical equilibrium and that the particle velocities are isotropic (which is not exactly realistic, e.g., Hansen & Moore 2006), a model for the density profile implies a particular form of the velocity dispersion, σ^2 , and the phase-space distribution function, $f(\varepsilon)$. The mathematical expressions for these quantities are given in Appendix D. The velocity dispersion can be measured in principle, e.g., from the motions of satellite galaxies or stars (Mamon et al. 2010; Okumura et al. 2018; Adhikari et al. 2019; Hamabata et al. 2019; Tomooka et al. 2020; Bose & Loeb 2021; Aung et al. 2021, 2022). We do not expect the dynamics to be fundamentally altered by the presence of baryons (Callingham et al. 2020).

In this section, we check whether the new model makes reasonable predictions for the dynamical quantities and we question whether other, energy-based models could make similar predictions. The former is not automatically guaranteed since not all profiles have positive, continuous distribution functions (Baes & Camps

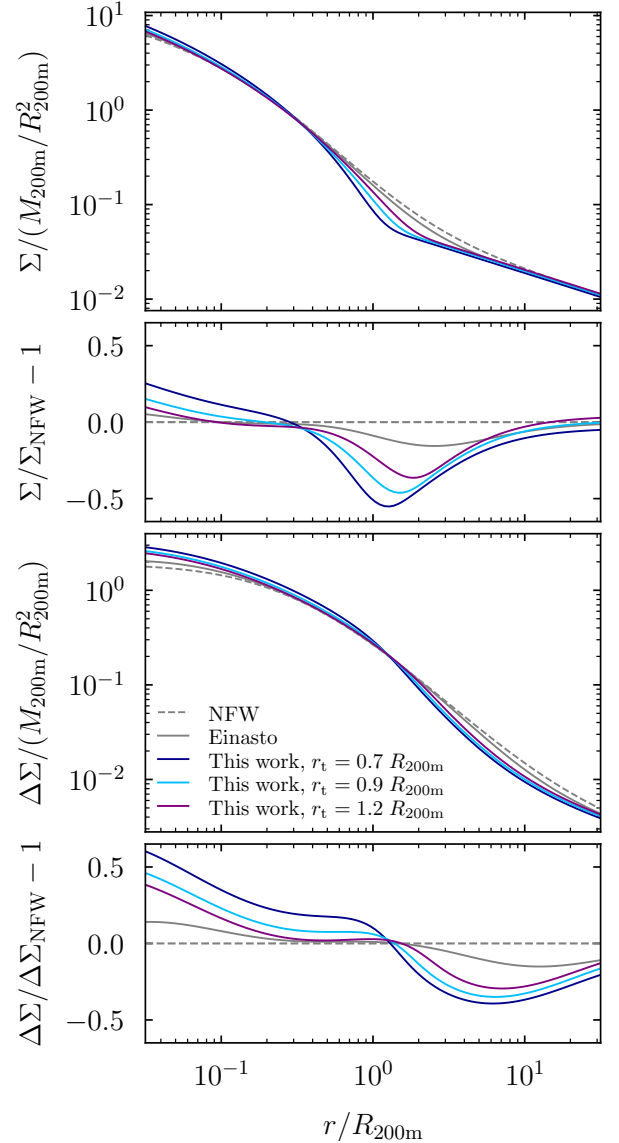


Figure 8. The projected (surface) density profile (top) and lensing signal (excess surface mass density, bottom) for characteristic profiles of a cluster halo with $M_{200\text{m}} = 5 \times 10^{14} h^{-1} M_{\odot}$ and $c_{200\text{m}} = 5$. We compare the NFW, Einasto, and truncated exponential profiles, where we force the truncation radius of the latter to the values listed in the legend and renormalize the profile to the same total mass. The differences in the transition region clearly propagate to the surface density profiles, where the different values of r_t are easily distinguishable by eye. The differences are smaller but propagate to a much larger radial range in $\Delta\Sigma$ because $\Sigma(r)$ is subtracted from the averaged surface density.

2021). We define $\psi(r)$ to be the (positive) gravitational potential of the halo and $\varepsilon \equiv \psi(r) - v^2/2$ to be the relative binding energy of particles. Particles with $\varepsilon < 0$ would be unbound and thus lead to $f(\varepsilon < 0) = 0$. Conversely, the maximum binding energy would correspond to particles that reside at the centre of the halo with velocity $v = 0$, meaning that $\varepsilon = \psi(0)$.

Fig. 9 shows radial profiles of density, enclosed mass, potential, and velocity dispersion, as well as the distribution function. We compare our new model (dark blue) to the NFW and Einasto forms (gray). The profiles are normalized to have the same total mass at the largest radius shown, and they are expressed in dimensionless units

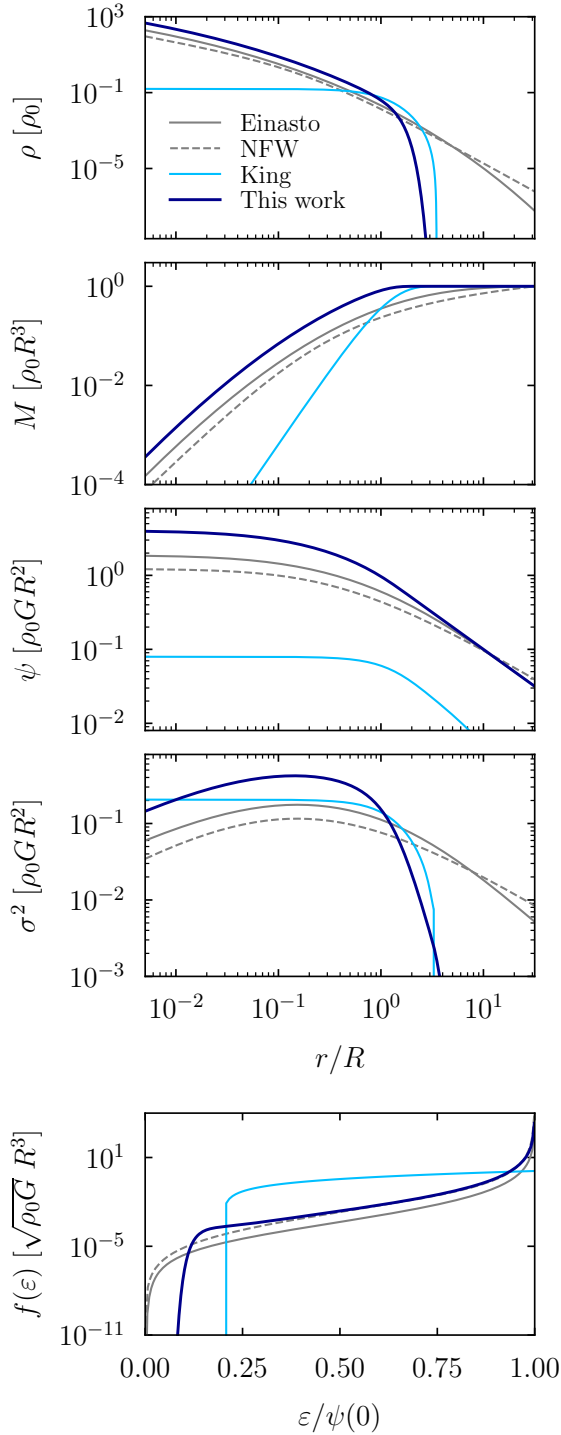


Figure 9. Dynamical properties of our new model (dark blue), a King (1966) profile (light blue, with a comparable cut-off radius), as well as the NFW and Einasto forms (gray). The panels show the density ρ , enclosed mass M , potential ψ , isotropic velocity dispersion σ^2 , and distribution function $f(\varepsilon)$ (from top to bottom). The latter falls to zero for unbound particles with $\varepsilon < 0$; conversely, $\varepsilon = \psi(0)$ corresponds to maximally bound particles at the centre of the halo. The profiles are expressed in dimensionless units and normalized to reach the same total mass $M = 1$ at the right edge of the plot. Compared to the conventional models, the sharp density cut-off in the new model leads to a mass distribution that suddenly flattens, a rapidly dropping velocity dispersion, and a sharp drop in the distribution function at the energy corresponding to orbits that reach their apocentre near the truncation radius.

rescaled by R , some scale density ρ_0 , and the gravitational constant G . The results thus depend only on the relative scales r_s/R and r_t/R , as well as the steepening parameters α and β . We choose a representative set of parameters for all models, namely $r_s/R = 0.2$, $\alpha = 0.18$, $r_t/R = 1$, and $\beta = 4$. We observe that $M(r)$ flattens as a consequence of the truncation in ρ , and that the potential approaches $\psi \propto 1/r$ at a smaller radius than for the Einasto profile.

The density cut-off is also mirrored in energy space, where the velocity dispersion falls sharply. The corresponding distribution function is similar to the NFW and Einasto profile at high binding energies, but it drops steeply at the binding energy corresponding to particles at the truncation radius. This is the desired behaviour for a profile that attempts to model the edge of the orbital distribution (e.g., King 1966; Drakos et al. 2017; Amorisco 2021). In other words, the splashback radius (the apocentre of the most recently accreted particles) is governed by a soft limit in the distribution of particle kinetic energies. Conversely, the NFW and Einasto profile have small, but finite, support out to the smallest binding energies (see also, e.g., Cardone et al. 2005; Mamon & Łokas 2005; Beraldo e Silva et al. 2014; Baes & Ciotti 2019). For large values of β such as 10 (i.e., very sharp truncation in density space), the distribution function can become non-monotonic near its cutoff.

These observations raise the questions of whether the truncation of the orbiting term could be described by a truncation of $f(\varepsilon)$ at some maximum energy. One well-known example of such models is the King (1966) family of profiles, which corresponds to an isothermal sphere that is sharply cut off at a certain binding energy (see also Michie 1963). This model is defined by the distribution function

$$f_{\text{king}}(\varepsilon) = f_0 \left(e^{(\varepsilon - \varepsilon_t)/\sigma^2} - 1 \right), \quad (16)$$

where f_0 is a normalization, σ the velocity dispersion of the isothermal sphere, and ε_t the energy where the object is truncated ($f \rightarrow 0$). We use the dimensionless variables of Drakos et al. (2017) to numerically integrate equation (16) to find the potential, density, and velocity dispersion profiles. Given our fundamental scale R and the mass normalization, the profile has only one free parameter $Z_t \equiv \varepsilon_t/[\sigma^2\psi(0)]$. The light-blue lines in Fig. 9 show a King profile with $Z_t = 0.2$, a cut-off energy chosen to roughly match the real-space truncation radius of $r_t = 0.2 R$. The position and sharpness of the truncation can be adjusted using Z_t (e.g., fig. 4.8 in Binney & Tremaine 2008), but Fig. 9 immediately explains why the King model cannot describe realistic halo profiles: the density approaches a large, fixed-density core at $r \ll R$. Moreover, the truncation in binding energy leads to a sharper real-space truncation than we observe in simulations. Our new model allows for lower binding energies (bottom panel) and thus for a smoother truncation.

Of course, the King model is only one example of dynamics-based profiles. Another recently suggested model is DARKexp (Hjorth & Williams 2010), but this model cannot fit the truncation because its slope approaches $\gamma = -4$ at large radii, regardless of the ϕ_0 parameter that controls the distribution of particle energies (Williams & Hjorth 2010; Williams et al. 2010). Similarly, Pontzen & Governato (2013) derive a distribution function by maximising the entropy, but it is not clear whether this model produces a truncation at the right radius (their fig. 7; see also Wagner 2020).

6 CONCLUSIONS

We have presented a new fitting function for halo density profiles, which is composed of models for the orbiting (one-halo) and infalling terms. The orbiting term is modelled as an extension of

the Einasto profile, $\rho_{\text{orb}} \propto \exp[-2/\alpha (r/r_s)^\alpha - 1/\beta (r/r_t)^\beta]$. The infalling term is a power law in density that smoothly approaches a maximum value at small radii. These functions are implemented in the publicly available COLLOSSUS code, including numerical routines for their mass, surface density, and $\Delta\Sigma$ integrals. Our main conclusions are as follows.

(i) The new model fits mean and median total profiles to roughly $\pm 5\%$ across a vast range of radius, halo mass, redshift, and cosmology. When halos are also selected by accretion rate, the fit quality can degrade to $\pm 20\%$ near the transition between the orbiting and infalling profiles.

(ii) The new model accurately fits the orbiting and infalling terms separately, even down to densities well below the cosmic mean. The exact fit quality depends on the chosen mass, accretion rate, and whether mean or median profiles are considered.

(iii) By fixing $\alpha = 0.18$ and $\beta = 3$, the orbiting model becomes a 3-parameter fit that captures the profiles of individual halos more accurately than Einasto profiles (on average).

(iv) The sharp truncation of the orbiting term corresponds to a truncation in the binding energy of particles, which is not replicated in more extended profile models.

(v) Different truncation radii lead to clear differences in the projected surface density profiles and in the lensing signal $\Delta\Sigma$.

(vi) We introduce an augmented ‘Model B’ that fixes the logarithmic slope at the scale radius to be -2 . This formulation is almost equivalent to the fiducial model but alleviates some rare parameter degeneracies at the cost of slightly increased complexity.

In Paper III, we will analyse the best-fit parameters of averaged and individual halo profiles. We have left a number of theoretical and practical questions unexplored. For example, we intend to provide analytical approximations for the mass and projected density of the new fitting function. Another urgent question is the relationship between the profile parameters and definitions of the halo boundary based on the orbiting population of subhalos (Aung et al. 2021; García et al. 2021), or other definitions based on the interplay between the infalling and orbiting components (Fong & Han 2021). Finally, we intend to apply the new model to observational data.

ACKNOWLEDGEMENTS

I am grateful to Nicole Drakos for help with computing King profiles and to Maarten Baes for verifying the dynamical properties of the new model. I thank Andrew Hearin and Keiichi Umetsu for comments on a draft, and Susmita Adhikari, Han Aung, Barun Dhar, Rafael Garcia, Daisuke Nagai, Eduardo Roza, and Angus Wright for productive conversations. This work was partially completed during the Coronavirus lockdown and would not have been possible without the essential workers who did not enjoy the privilege of working from the safety of their homes. The computations were run on the MIDWAY computing cluster provided by the University of Chicago Research Computing Center and on the DeepThought2 cluster at the University of Maryland. This research extensively used the python packages NUMPY (Harris et al. 2020), SCIPY (Virtanen et al. 2020), MATPLOTLIB (Hunter 2007), and COLLOSSUS (Diemer 2018).

DATA AVAILABILITY

The SPARTA code that was used to extract the dynamically split density profiles from our simulations is publicly available in a BitBucket

repository, bitbucket.org/bdiemer/sparta. An extensive online documentation can be found at bdiemer.bitbucket.io/sparta. The SPARTA output files (one file per simulation) are available in an hdf5 format at erebos.astro.umd.edu/erebos/sparta. A Python module to read these files is included in the SPARTA code. Additional figures are provided online on the author’s website at benediktdiemer.com/data. The full particle data for the Erebus N -body simulations are too large to be permanently hosted online, but they are available upon request.

REFERENCES

- Adhikari S., Dalal N., Chamberlain R. T., 2014, *JCAP*, **11**, 19
 Adhikari S., Dalal N., More S., Wetzel A., 2019, *ApJ*, **878**, 9
 Adhikari S., et al., 2021, *ApJ*, **923**, 37
 Amorisco N. C., 2021, arXiv e-prints, p. [arXiv:2111.01148](https://arxiv.org/abs/2111.01148)
 An J., Zhao H., 2013, *MNRAS*, **428**, 2805
 Aung H., Nagai D., Roza E., García R., 2021, *MNRAS*, **502**, 1041
 Aung H., Nagai D., Roza E., Wolfe B., Adhikari S., 2022, arXiv e-prints, p. [arXiv:2204.13131](https://arxiv.org/abs/2204.13131)
 Baes M., Camps P., 2021, *MNRAS*, **503**, 2955
 Baes M., Ciotti L., 2019, *A&A*, **626**, A110
 Baltz E. A., Marshall P., Oguri M., 2009, *J. Cosmology Astropart. Phys.*, **1**, 15
 Baxter E., et al., 2017, *ApJ*, **841**, 18
 Becker M. R., Kravtsov A. V., 2011, *ApJ*, **740**, 25
 Behroozi P. S., Wechsler R. H., Wu H.-Y., 2013a, *ApJ*, **762**, 109
 Behroozi P. S., Wechsler R. H., Wu H.-Y., Busha M. T., Klypin A. A., Primack J. R., 2013b, *ApJ*, **763**, 18
 Beraldo e Silva L., Lima M., Sodré L., Perez J., 2014, *Phys. Rev. D*, **90**, 123004
 Bertschinger E., 1985, *ApJS*, **58**, 39
 Betancort-Rijo J. E., Sanchez-Conde M. A., Prada F., Patiri S. G., 2006, *ApJ*, **649**, 579
 Bianconi M., Buscicchio R., Smith G. P., McGee S. L., Haines C. P., Finoguenov A., Babul A., 2021, *ApJ*, **911**, 136
 Binney J., 1982, *MNRAS*, **200**, 951
 Binney J., Tremaine S., 2008, *Galactic Dynamics: Second Edition*. Princeton University Press
 Bond J. R., Kofman L., Pogossyan D., 1996, *Nature*, **380**, 603
 Bose S., Loeb A., 2021, *ApJ*, **912**, 114
 Brown S. T., McCarthy I. G., Diemer B., Font A. S., Stafford S. G., Pfiefer S., 2020, *MNRAS*, **495**, 4994
 Burkert A., 1995, *ApJ*, **447**, L25
 Callingham T. M., Cautun M., Deason A. J., Frenk C. S., Grand R. J. J., Marinacci F., Pakmor R., 2020, *MNRAS*, **495**, 12
 Cardone V. F., Piedipalumbo E., Tortora C., 2005, *MNRAS*, **358**, 1325
 Chang C., et al., 2018, *ApJ*, **864**, 83
 Cooray A., Sheth R., 2002, *Phys. Rep.*, **372**, 1
 Courteau S., et al., 2014, *Reviews of Modern Physics*, **86**, 47
 Crocce M., Pueblas S., Scoccimarro R., 2006, *MNRAS*, **373**, 369
 Dacunha T., Belyakov M., Adhikari S., Shin T.-h., Goldstein S., Jain B., 2022, *MNRAS*, **512**, 4378
 Dehnen W., 1993, *MNRAS*, **265**, 250
 Dekel A., Ishai G., Dutton A. A., Maccio A. V., 2017, *MNRAS*, **468**, 1005
 Dhar B. K., 2021, *MNRAS*, **504**, 4583
 Dhar B. K., Williams L. L. R., 2010, *MNRAS*, **405**, 340
 Di Cintio A., Brook C. B., Macciò A. V., Stinson G. S., Knebe A., Dutton A. A., Wadsley J., 2014, *MNRAS*, **437**, 415
 Diemand J., Kuhlen M., 2008, *ApJ*, **680**, L25
 Diemer B., 2017, *ApJS*, **231**, 5
 Diemer B., 2018, *The Astrophysical Journal Supplement Series*, **239**, 35
 Diemer B., 2020, *ApJS*, **251**, 17
 Diemer B., 2022, *MNRAS*, **513**, 573
 Diemer B., Kravtsov A. V., 2014, *ApJ*, **789**, 1
 Diemer B., Kravtsov A. V., 2015, *ApJ*, **799**, 108
 Diemer B., More S., Kravtsov A. V., 2013, *ApJ*, **766**, 25

- Dooley G. A., Griffen B. F., Zukin P., Ji A. P., Vogelsberger M., Hernquist L. E., Frebel A., 2014, *ApJ*, **786**, 50
- Doroshkevich A. G., Shandarin S. F., 1978, *Soviet Ast.*, **22**, 653
- Drakos N. E., Taylor J. E., Benson A. J., 2017, *MNRAS*, **468**, 2345
- Dubinski J., Carlberg R. G., 1991, *ApJ*, **378**, 496
- Dutton A. A., Macciò A. V., 2014, *MNRAS*, **441**, 3359
- Eckert D., Ettori S., Robertson A., Massey R., Pointecouteau E., Harvey D., McCarthy I. G., 2022, *A&A*, **666**, A41
- Eddington A. S., 1916, *MNRAS*, **76**, 572
- Efstathiou G., Frenk C. S., White S. D. M., Davis M., 1988, *MNRAS*, **235**, 715
- Einasto J., 1965, *Trudy Astrofizicheskogo Instituta Alma-Ata*, **5**, 87
- Einasto J., 1969, *Astrophysics*, **5**, 67
- Erwin P., 2015, *ApJ*, **799**, 226
- Fielder C. E., Mao Y.-Y., Zentner A. R., Newman J. A., Wu H.-Y., Wechsler R. H., 2020, *MNRAS*, **499**, 2426
- Fong M., Han J., 2021, *MNRAS*, **503**, 4250
- Freundlich J., et al., 2020, *MNRAS*, **499**, 2912
- Fukushige T., Makino J., 2001, *ApJ*, **557**, 533
- Gao L., Navarro J. F., Cole S., Frenk C. S., White S. D. M., Springel V., Jenkins A., Neto A. F., 2008, *MNRAS*, **387**, 536
- García R., Rozo E., Becker M. R., More S., 2021, *MNRAS*, **505**, 1195
- García R., Salazar E., Rozo E., Adhikari S., Aung H., Diemer B., Nagai D., Wolfe B., 2022, *arXiv e-prints*, p. [arXiv:2207.11827](https://arxiv.org/abs/2207.11827)
- Genina A., et al., 2018, *MNRAS*, **474**, 1398
- Ghigna S., Moore B., Governato F., Lake G., Quinn T., Stadel J., 2000, *ApJ*, **544**, 616
- Graham A. W., Merritt D., Moore B., Diemand J., Terzić B., 2006, *AJ*, **132**, 2701
- Gunn J. E., Gott III J. R., 1972, *ApJ*, **176**, 1
- Hamabata A., Oguri M., Nishimichi T., 2019, *MNRAS*, **489**, 1344
- Hansen S. H., Moore B., 2006, *New Astron.*, **11**, 333
- Harris C. R., et al., 2020, *Nature*, **585**, 357
- Hernquist L., 1990, *ApJ*, **356**, 359
- Hjorth J., Williams L. L. R., 2010, *ApJ*, **722**, 851
- Hunter J. D., 2007, *Computing in Science Engineering*, **9**, 90
- Jaffe W., 1983, *MNRAS*, **202**, 995
- King I. R., 1966, *AJ*, **71**, 64
- Klypin A. A., Trujillo-Gomez S., Primack J., 2011, *ApJ*, **740**, 102
- Klypin A., Yepes G., Gottlöber S., Prada F., Heß S., 2016, *MNRAS*, **457**, 4340
- Knollmann S. R., Power C., Knebe A., 2008, *MNRAS*, **385**, 545
- Komatsu E., et al., 2011, *ApJS*, **192**, 18
- Lazar A., et al., 2020, *MNRAS*, **497**, 2393
- Lewis A., Challinor A., Lasenby A., 2000, *ApJ*, **538**, 473
- Lilley E. J., Evans N. W., Sanders J. L., 2018, *MNRAS*, **476**, 2086
- Łokas E. L., Mamon G. A., 2001, *MNRAS*, **321**, 155
- Lucie-Smith L., Peiris H. V., Pontzen A., Nord B., Thiyagalingam J., Piras D., 2022a, *Phys. Rev. D*, **105**, 103533
- Lucie-Smith L., Adhikari S., Wechsler R. H., 2022b, *MNRAS*, **515**, 2164
- Ludlow A. D., Angulo R. E., 2017, *MNRAS*, **465**, L84
- Ludlow A. D., Navarro J. F., White S. D. M., Boylan-Kolchin M., Springel V., Jenkins A., Frenk C. S., 2011, *MNRAS*, **415**, 3895
- Ludlow A. D., et al., 2013, *MNRAS*, **432**, 1103
- Ludlow A. D., Bose S., Angulo R. E., Wang L., Hellwing W. A., Navarro J. F., Cole S., Frenk C. S., 2016, *MNRAS*, **460**, 1214
- Ludlow A. D., Schaye J., Bower R., 2019, *MNRAS*, **488**, 3663
- Mamon G. A., Łokas E. L., 2005, *MNRAS*, **362**, 95
- Mamon G. A., Biviano A., Murante G., 2010, *A&A*, **520**, A30
- Mansfield P., Avestruz C., 2021, *MNRAS*, **500**, 3309
- Merritt D., Graham A. W., Moore B., Diemand J., Terzić B., 2006, *AJ*, **132**, 2685
- Michie R. W., 1963, *MNRAS*, **125**, 127
- Moore B., Quinn T., Governato F., Stadel J., Lake G., 1999, *MNRAS*, **310**, 1147
- More S., Diemer B., Kravtsov A. V., 2015, *ApJ*, **810**, 36
- More S., et al., 2016, *ApJ*, **825**, 39
- Murata R., Sunayama T., Oguri M., More S., Nishizawa A. J., Nishimichi T., Osato K., 2020, *PASJ*, **72**, 64
- Navarro J. F., Frenk C. S., White S. D. M., 1995, *MNRAS*, **275**, 720
- Navarro J. F., Frenk C. S., White S. D. M., 1996, *ApJ*, **462**, 563
- Navarro J. F., Frenk C. S., White S. D. M., 1997, *ApJ*, **490**, 493
- Navarro J. F., et al., 2004, *MNRAS*, **349**, 1039
- Navarro J. F., et al., 2010, *MNRAS*, **402**, 21
- O'Donnell C., Behroozi P., More S., 2022, *MNRAS*, **509**, 3285
- O'Neil S., Barnes D. J., Vogelsberger M., Diemer B., 2021, *MNRAS*, **504**, 4649
- O'Neil S., Borrow J., Vogelsberger M., Diemer B., 2022, *MNRAS*, **513**, 835
- Oguri M., Hamana T., 2011, *MNRAS*, **414**, 1851
- Okumura T., Nishimichi T., Umetsu K., Osato K., 2018, *Phys. Rev. D*, **98**, 023523
- Peng C. Y., Ho L. C., Impey C. D., Rix H.-W., 2010, *AJ*, **139**, 2097
- Planck Collaboration et al., 2014, *A&A*, **571**, A16
- Pontzen A., Governato F., 2013, *MNRAS*, **430**, 121
- Power C., Navarro J. F., Jenkins A., Frenk C. S., White S. D. M., Springel V., Stadel J., Quinn T., 2003, *MNRAS*, **338**, 14
- Prada F., Klypin A. A., Simonneau E., Betancort-Rijo J., Patiri S., Gottlöber S., Sanchez-Conde M. A., 2006, *ApJ*, **645**, 1001
- Read J. I., Agertz O., Collins M. L. M., 2016, *MNRAS*, **459**, 2573
- Retana-Montenegro E., van Hese E., Gentile G., Baes M., Frutos-Alfaro F., 2012, *A&A*, **540**, A70
- Ricotti M., Pontzen A., Viel M., 2007, *ApJ*, **663**, L53
- Schneider A., Teyssier R., Stadel J., Chisari N. E., Le Brun A. M. C., Amara A., Refregier A., 2019, *J. Cosmology Astropart. Phys.*, **2019**, 020
- Shapiro P. R., Iliev I. T., Raga A. C., 1999, *MNRAS*, **307**, 203
- Shin T.-h., Diemer B., 2022, *arXiv e-prints*, p. [arXiv:2210.14262](https://arxiv.org/abs/2210.14262)
- Shin T., et al., 2019, *MNRAS*, **487**, 2900
- Shin T., et al., 2021, *MNRAS*, **507**, 5758
- Springel V., 2005, *MNRAS*, **364**, 1105
- Springel V., White S. D. M., 1999, *MNRAS*, **307**, 162
- Stadel J., Potter D., Moore B., Diemand J., Madau P., Zemp M., Kuhlen M., Quilis V., 2009, *MNRAS*, **398**, L21
- Sugiura H., Nishimichi T., Rasera Y., Taruya A., 2020, *MNRAS*, **493**, 2765
- Tasitsiomi A., Kravtsov A. V., Gottlöber S., Klypin A. A., 2004, *ApJ*, **607**, 125
- Tavio H., Cuesta A. J., Prada F., Klypin A. A., Sanchez-Conde M. A., 2008, *arXiv:0807.3027*,
- Teyssier R., Pontzen A., Dubois Y., Read J. I., 2013, *MNRAS*, **429**, 3068
- Tomooka P., Rozo E., Wagoner E. L., Aung H., Nagai D., Safonova S., 2020, *MNRAS*, **499**, 1291
- Udrescu S. M., Dutton A. A., Macciò A. V., Buck T., 2019, *MNRAS*, **482**, 5259
- Umetsu K., 2020, *A&ARv*, **28**, 7
- Umetsu K., Diemer B., 2017, *ApJ*, **836**, 231
- Velliscig M., van Daalen M. P., Schaye J., McCarthy I. G., Cacciato M., Le Brun A. M. C., Vecchia C. D., 2014, *MNRAS*, **442**, 2641
- Virtanen P., et al., 2020, *Nature Methods*, **17**, 261
- Wagner J., 2020, *General Relativity and Gravitation*, **52**, 61
- Wang J., Bose S., Frenk C. S., Gao L., Jenkins A., Springel V., White S. D. M., 2020, *Nature*, **585**, 39
- Wechsler R. H., Tinker J. L., 2018, *ARA&A*, **56**, 435
- Wechsler R. H., Bullock J. S., Primack J. R., Kravtsov A. V., Dekel A., 2002, *ApJ*, **568**, 52
- Williams L. L. R., Hjorth J., 2010, *ApJ*, **722**, 856
- Williams L. L. R., Hjorth J., Wojtak R., 2010, *ApJ*, **725**, 282
- Khakaj E., Diemer B., Leauthaud A., Wasserman A., Huang S., Luo Y., Adhikari S., Singh S., 2020, *MNRAS*, **499**, 3534
- Khakaj E., Leauthaud A., Lange J., Hearin A., Diemer B., Dalal N., 2022, *MNRAS*, **514**, 2876
- Zhao H., 1996, *MNRAS*, **278**, 488
- Zhao D. H., Jing Y. P., Mo H. J., Börner G., 2009, *ApJ*, **707**, 354
- de Blok W. J. G., 2010, *Advances in Astronomy*, **2010**, 789293

APPENDIX A: DETAILS ON FITTING PROCEDURE

In this Appendix, we give additional detail on the technical aspects of our profile fits. In Section A1 we discuss our fitting procedure and in Section A2 we describe the reasoning behind and meaning of the parameter limits given in Section 2.7 and Table 1.

A1 Fitting procedure

A first important choice is the definition of the residual. The conventional approach of minimizing the square of $(\rho_{\text{fit}} - \rho_{\text{data}})/\sigma$ works poorly in the outer profiles because the summed χ^2 is dominated by the much higher densities at small radii. Some authors have chosen to minimize $r^2(\rho_{\text{fit}} - \rho_{\text{data}})/\sigma$ instead, but this function still represents an arbitrary weighting with radius. One can even fit the slope profile, but the results depend on how the slope is estimated from noisy data (O’Neil et al. 2021). To obtain a fit of equal quality at all radii, we minimize the square logarithmic differences between simulated and fitted profiles. We find that we obtain the most physically sensible fits if we aggressively reduce the effect of outliers by using a Cauchy loss function, so that the minimized quantity is

$$\chi_{\text{cauchy}}^2 \equiv \sum_i \ln(1 + \chi_i^2) \quad \text{with} \quad \chi_i \equiv \frac{\ln \rho_{i,\text{fit}} - \ln \rho_{i,\text{data}}}{\ln(1 + \sigma_i/\rho_{i,\text{data}})}, \quad (\text{A1})$$

where $\rho_{i,\text{fit}}$ is the fit density in bin i , $\rho_{i,\text{data}}$ is the density of the simulated profile (individual or averaged), and σ_i is the uncertainty in $\rho_{i,\text{data}}$. Throughout the paper, we quote the usual values of $\chi^2 = \sum \chi_i^2$, i.e., the logarithmic differences without taking the loss function into account. The additional logarithm in the Cauchy loss function allows the fitter to ignore features such as wiggles in favour of a better fit to the well-defined inner profile.

The next decision is how to define the uncertainty σ_i of each profile bin. The bootstrap estimate, σ_{bs} , captures statistical variations in averaged profiles, but it does not account for systematic errors that could arise from numerics, from our profile splitting algorithm, from baryonic effects, and (perhaps most importantly) from substructure. We crudely account for such errors by adding a systematic uncertainty of 5% in quadrature,

$$\sigma_{i,\text{mean/median}} = \sqrt{\sigma_{i,\text{bs}}^2 + \sigma_{\text{sys,av}}^2} = \sqrt{\sigma_{i,\text{bs}}^2 + (0.05 \rho_{i,\text{data}})^2}. \quad (\text{A2})$$

The systematic error does have some effect on the best-fit profiles and parameters. It essentially represents a trade-off: if its value is small, the fit ‘trusts’ the statistically well-constrained inner profile over the noisier transition region; if its value is large, all bins are weighted more or less equally. Given that the tests in Paper I demonstrated convergence to roughly 5% accuracy, this value is a reasonable approximation to the systematic uncertainty.

We minimize χ^2 using the ‘trust region reflective’ (trf) algorithm of the least-squares function in `scipy`. We find this algorithm to converge more reliably than the similar ‘dogbox’ variant. Both methods are faster than a conventional Levenberg-Marquardt solver and allow us to impose the parameter limits listed in Table 1. All parameters are fit in log space to avoid zero or negative values. Despite these optimizations, any steepest-gradient solver is liable to ‘fall into’ the first local minimum in χ^2 it encounters, which may be far from the global minimum. We avoid false minima with the following procedure. We begin from a fiducial initial guess and run the fitter with a relatively low relative target accuracy of 10^{-3} . Using the output as a starting point, we vary the initial guess of each parameter to its extremes, that is, fractions of 0.05 and 0.95 between its lower and upper bounds in log space. If the resulting fit improves on the previous χ^2 , we set the new results as the initial guess. If the total

gradient at the solution (‘optimality’) is larger than 10^{-3} , we repeat the procedure for more initial guesses of the parameter in question, namely fractions of [0.2, 0.35, 0.5, 0.65, 0.8] of its allowed log interval. Once all parameters have been varied, we accept the initial guess that resulted in the lowest χ^2 of all attempts and re-run the fit with a higher accuracy of 10^{-5} to obtain the final result. At modest cost, this algorithm ensures that virtually all fits converge to a reasonable solution and that the results are independent of the initial guess. The values for χ^2/N_{dof} when fitting the averaged orbiting term hover around unity, though with a large spread that depends on the sample selection and whether we fit mean or median. When fitting the total profiles, χ^2/N_{dof} roughly ranges between 0.01 and 1.

Fitting individual halo profiles can be particularly challenging because substructure and halo-to-halo scatter can lead to significant deviations from any fitting function (e.g., Umetsu & Diemer 2017). We thus slightly adjust the procedure laid out in the previous section for individual halo fits, as well as the parameter ranges (Table 1). Since the simulations do not provide a meaningful estimate of the uncertainty on individual profiles, we assume a Poisson-like statistical uncertainty due to the number of particles as a minimum,

$$\sigma_{i,\text{ind}} = \rho_{i,\text{data}} \sqrt{\frac{1}{N_{i,\text{ptl}}} + \sigma_{\text{sys,ind}}^2}, \quad (\text{A3})$$

where $N_{i,\text{ptl}}$ is the number of particles in the given bin and $\sigma_{\text{sys,ind}}$ is a fixed systematic error. Since most bins contain $N_{i,\text{ptl}} \gg 1$ particles, the normalization of χ^2 is largely determined by the somewhat arbitrary value for $\sigma_{\text{sys,ind}}$. This systematic error term effectively weighs bins with low particle number against well-resolved bins because all bins with $N_{i,\text{ptl}} \gg 1/\sigma_{\text{sys,ind}}^2$ receive roughly the same weight in the fit. This method prevents the fit from being dominated by a few bins with high N_{ptl} . We set $\sigma_{\text{sys,ind}} = 0.25$, meaning that the systematic error dominates for bins with $N_{i,\text{ptl}} > 16$. With this value, the median χ^2/N_{dof} ranges from 0.5 to 2 for the different halo samples. We have verified that the choice of systematic error does not greatly influence the overall distribution of the best-fit parameters.

A2 Parameter Limits

The normalization, ρ_s , is tightly related to the formation redshift of halos (Navarro et al. 1997; Ludlow et al. 2013) and thus cannot vary arbitrarily. Nonetheless, we allow a generous range because ρ_s is well-constrained in all fits. If we instead use the density at the centre, ρ_0 , by setting $C = 0$ in Section 2.4, some parameter combinations can extrapolate to extreme central densities and the limits need to be much more flexible (Table 1).

Some profiles steepen so slowly that they exhibit no true scale radius, i.e., $\gamma \approx -2$ over a wide range of radii. In such cases, the fit tends to shift r_s towards large values that can even exceed r_t , which is technically a valid solution because of the symmetry between the r_s and r_t terms in equation (9). After extensive experimentation, we find it necessary to enforce the correct, physical ordering of the terms by explicitly requiring $r_t > r_s$. In particular, we set $0.01 < r_s/R_{200\text{m}} < 0.45$ and $0.5 < r_t/R_{200\text{m}} < 3$. The range of r_s limits the concentration to $2.2 < c_{200\text{m}} < 100$, but halos outside of this range would correspond to extreme outliers in the population (e.g., Diemer & Kravtsov 2015); we never observe a preference for $r_s \gtrsim 0.4 R_{200\text{m}}$ in well-constrained fits. The lower limit corresponds roughly to the lowest radii where our averaged profiles are resolved, meaning that r_s cannot be measured reliably near $0.01 R_{200\text{m}}$. This limit could be revisited with high-resolution simulations that probe smaller radii. Similarly, we do not observe a truncation at

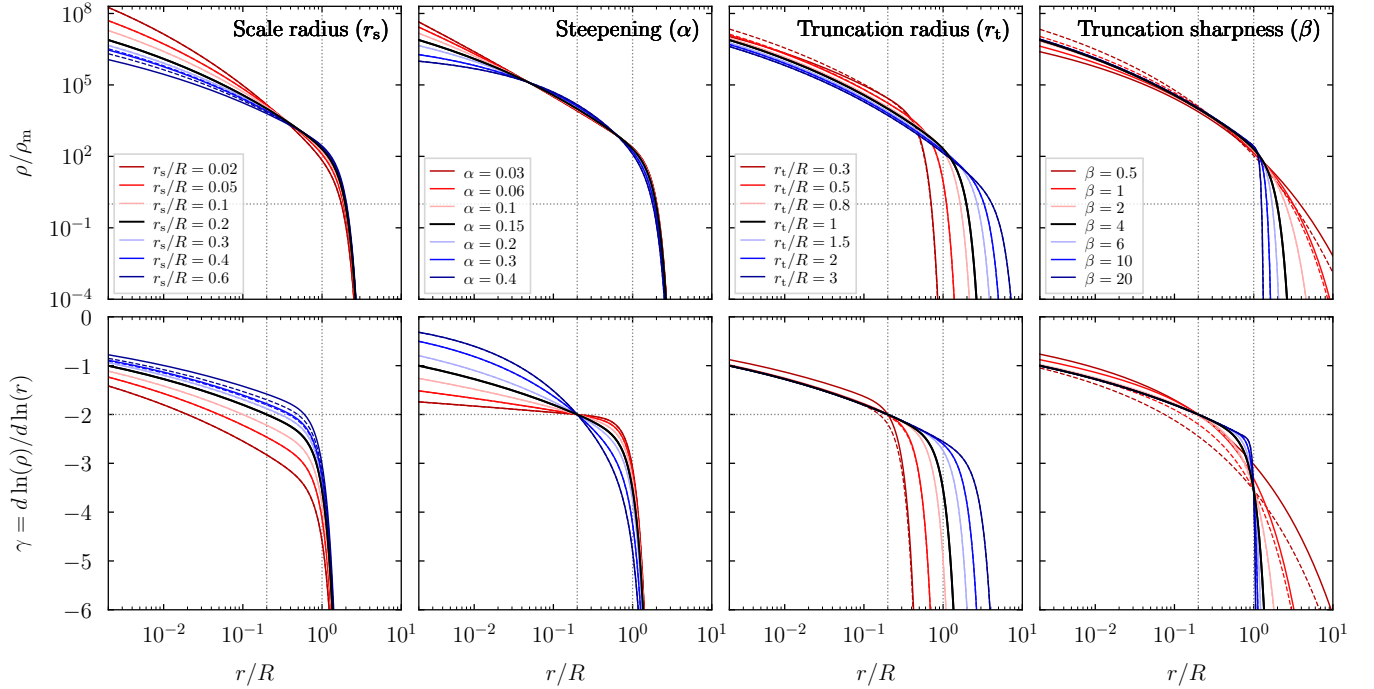


Figure A1. Same as Fig. 1, but showing the modified Model B with $\eta = 0.1$ (solid lines) and a comparison to our fiducial Model A (equation (9), dashed lines). Wherever the dashed lines are invisible, the models make indistinguishable predictions. The most important differences occur in the right two columns. While Model B fixes the slope at $\gamma(r_s) = -2$ regardless of the values of r_t and β , Model A can exhibit slight deviations from this value if r_t and/or β are small.

radii smaller than $0.5 R_{200m}$ in any profiles, and we generally find little evidence for $r_t > 2 R_{200m}$. If r_t pushes against the upper limit, the profile does not experience a clear truncation, meaning that the values of r_t and β are arbitrary. We have experimented with falling back on an Einasto fit in such cases, but the fit quality is almost always degraded, which demonstrates that almost all orbiting profiles experience some steepening beyond that of the Einasto slope.

For the steepening parameter, we allow $0.03 < \alpha < 0.4$, the most extreme values that could reasonably be ascribed to any profiles we have tested. The lower limit corresponds to an almost invariant slope near -2 , which is the case for some halos with high accretion rates (Paper I). The Einasto profile can suffer from a well-known degeneracy between r_s and α if profiles do not extend to small radii or if their slope evolves slowly with radius (e.g., Ricotti et al. 2007; Udrescu et al. 2019). While virtually all averaged profiles do constrain α to some extent, most individual halo profiles do not. In particular, the average fit quality remains roughly constant within the range $0.1 < \alpha < 0.2$, highlighting that individual profiles simply do not contain sufficient information to determine α . We could set it based on an ν - α relation (Gao et al. 2008; Klypin et al. 2016), but these trends with peak height turn out to be an artefact of the Einasto form poorly fitting the true, truncated profiles (Paper III). Instead, we find that $\alpha \approx 0.18$ in most averaged profiles, and that it depends on the accretion rate (Paper III) and on the slope of the linear power spectrum (Paper I; Ludlow & Angulo 2017; Brown et al. 2020). While the profiles of individual halos with very high Γ do indeed show a mild preference for low α , the differences in fit quality are modest at best. Thus, we simply fix $\alpha = 0.18$ in all fits to individual profiles. This value leads to concentrations that are similar to those measured using NFW profiles (Dutton & Macciò 2014; Ludlow et al. 2016), but other choices have been made in the literature (e.g., $\alpha = 0.16$, Wang et al. 2020).

We have no intuitive prior for the transition sharpness β , but the profiles shown in Paper I range from gradual to very sharp transitions. Thus, we allow β to fluctuate between 0.1 and 10. While some fits technically prefer even larger values, those correspond to an essentially instantaneous cut-off, where β is not well defined. We might worry that the r_t - β term suffers from a degeneracy similar to that of the r_s - α term, but we find that r_t and β are not intrinsically degenerate and both well-constrained for most averaged profiles (Paper III). In individual halos, however, the orbiting profiles commonly become unresolved at the radii that most constrain β . We thus fix $\beta = 3$, which barely decreases the average fit quality of the total profiles. To accommodate profiles that do not exhibit any noticeable truncation, we allow the truncation radius to shift to very large values where it does not matter, $r_t/R_{200m} \leq 10$.

In the infalling profile, we limit the normalization to $1 < \delta_1 < 100$. Added to the mean density of the Universe, the lower limit corresponds to $\rho_{inf}(R_{200m}) = 2\rho_m$. Such low overdensities are observed in the self-similar simulation with $n = -1$. We leave the slope to fluctuate between $0.01 < s < 4$, which includes any reasonable (positive) value encountered in simulated profiles. The asymptotic central overdensity δ_{max} reaches values between 10 and 1000 in the profiles where it is constrained, but we allow $1 < \delta_{max} < 10^4$ to allow for profiles that do not exhibit a measurable maximum. We apply the limits discussed so far in the separate fits to the orbiting and infalling profile components. When we combine them to fit the total profiles, we do not vary δ_{max} because the infalling profile is subdominant to the orbiting term at $r < R_{200m}$, meaning that δ_{max} is unconstrained. In a situation where only the total profile is known, δ_{max} can be set to a reasonable value (e.g., 500) without a significant impact on the fit.

APPENDIX B: MODEL VARIANT WITH CORRECTION AT SCALE RADIUS

In Section 2.4, we noted that the truncation term in equation (9) has the undesirable effect of breaking the $\gamma(r_s) = -2$ condition. We now construct a model variant that maintains this condition, which we call Model B (in contrast to the fiducial model, which we shall call Model A for brevity). We wish to introduce a new term in the slope that enforces $\gamma(r_s) = -2$, but we need to be careful. For example, if we add $(r_s/r_t)^\beta$ into the slope of Model A, $\gamma(r)$ is still integrable and adds the term $(r_s/r_t)^\beta \ln(r)$ to $S(r)$ from equation (7). While this new model would now satisfy $\gamma(r_s) = -2$, γ has been renormalized at all radii with a fixed term that survives all the way to the centre of the halo, $\gamma(0) = (r_s/r_t)^\beta$. This feature is highly undesirable because it ties the central slope to the entirely unrelated properties of the truncation term. Instead, we introduce a multiplicative term that vanishes at $r = 0$ and approaches $(r_s/r_t)^\beta$ at $r = r_s$,

$$\gamma(r) = -2 \left(\frac{r}{r_s} \right)^\alpha - \left(\frac{r}{r_t} \right)^\beta + \left(\frac{r_s}{r_t} \right)^\beta \left(\frac{r}{r_s} \right)^\eta. \quad (\text{B1})$$

We integrate γ/r to find

$$S(r) = -\frac{2}{\alpha} \left(\frac{r}{r_s} \right)^\alpha - \frac{1}{\beta} \left(\frac{r}{r_t} \right)^\beta + \frac{1}{\eta} \left(\frac{r_s}{r_t} \right)^\beta \left(\frac{r}{r_s} \right)^\eta + C. \quad (\text{B2})$$

Once again, we can set $C = 0$ or ensure $S(r_s) = 0$ by setting

$$C = \frac{2}{\alpha} + \left[\frac{1}{\beta} - \frac{1}{\eta} \right] \left(\frac{r_s}{r_t} \right)^\beta, \quad (\text{B3})$$

which causes the familiar extra terms from equations (4) and (7),

$$S = -\frac{2}{\alpha} \left[\left(\frac{r}{r_s} \right)^\alpha - 1 \right] - \frac{1}{\beta} \left[\left(\frac{r}{r_t} \right)^\beta - \left(\frac{r_s}{r_t} \right)^\beta \right] + \frac{1}{\eta} \left(\frac{r_s}{r_t} \right)^\beta \left[\left(\frac{r}{r_s} \right)^\eta - 1 \right]. \quad (\text{B4})$$

While this form looks somewhat complicated, it has a straightforward interpretation: its slope is renormalized to match -2 at the scale radius but this normalization factor decays towards $r = 0$. Here, η is a nuisance parameter that determines how fast this decay happens: the larger η , the faster the slope approaches zero at small radii. On the other hand, η also introduces an undesirable change in the slope at larger radii (where $r/r_s \gtrsim r_s/r_t$). However, as long as $\beta \gg 1$ and $\eta < 1$, this correction is barely noticeable. We fix $\eta = 0.1$, but the Model B fits are insensitive in the range $0.01 < \eta < 0.2$. In some fits to mean orbiting-only profiles, the best-fit value of α depends slightly on η , but this dependence disappears when fitting the entire profile or median orbiting profiles.

Fig. A1 shows the impact of different parameter values on Model B and highlights differences to Model A as dashed lines. As expected, Model B produces profiles that are indistinguishable from Model A for all but the most extreme parameter values. Differences are apparent for small r_t and/or small β . The example of $r_t/R_{200m} = 0.3$ is outside of the allowed parameter range for our fits ($r_t \geq 0.5R_{200m}$), but we do allow very small values of β . Model A fixes the slope at r_t to be $\gamma(r_t) = -2(r_t/r_s)^\alpha - 1$, which lies between -3 and -4 for most parameter values. Conversely, Model B fixes the slope at r_s to be $\gamma = -2$ regardless of the other parameters, but the slope at r_t becomes $\gamma(r_t) = -2(r_t/r_s)^\alpha - 1 + (r_t/r_s)^{\eta-\beta}$. The β -dependent correction term is negligible except for the smallest β .

The advantage of Model B is that r_s takes on its usual meaning as the radius where $\gamma = -2$, which avoids parameter degeneracies in power law-like profiles where the scale radius is poorly constrained (Paper I). We have, however, verified that models A and B are indistinguishable for virtually all mean and median profile fits. Wherever there are small differences, Model B tends to fit slightly better. The

most significant differences in the best-fit parameters occur for r_s in low- Γ averaged samples and in some individual halo profiles. The values of r_t and β are almost never affected, except in ill-defined fits. In summary, Model B is, fundamentally, the same profile model as Model A, and the best-fit parameters do not depend on the model except in some pathological cases. While we have exclusively shown Model A fits throughout this paper, we will also investigate best-fit parameters from Model B in Paper III.

APPENDIX C: DERIVATIVES WITH RESPECT TO PARAMETERS

Least-squares fits are often faster and more reliable if the user provides derivatives of the fitted function with respect to its free parameters θ . For orbiting profiles that follow the form $\rho = \rho_s e^{S(r)}$, those derivatives become

$$\frac{d \ln \rho}{d \ln \theta} = \theta \frac{dS}{d\theta}. \quad (\text{C1})$$

The derivative with respect to the normalisation is $d \ln \rho / d \ln \rho_s = 1$ regardless of $S(r)$, and we thus do not repeat it for the models listed below. We have double-checked the following expressions numerically and against Wolfram Alpha.

C1 Orbiting: Einasto

If we set $C = 0$, the derivatives with respect to the parameters are

$$\begin{aligned} \frac{d \ln \rho}{d \ln r_s} &= 2 \left(\frac{r}{r_s} \right)^\alpha \\ \frac{d \ln \rho}{d \ln \alpha} &= \frac{2}{\alpha} \left(\frac{r}{r_s} \right)^\alpha \left[1 - \alpha \ln \left(\frac{r}{r_s} \right) \right]. \end{aligned} \quad (\text{C2})$$

If we set $C = 2/\alpha$ as in equation (4), the derivative with respect to r_s remains the same but

$$\frac{d \ln \rho}{d \ln \alpha} = \frac{2}{\alpha} \left[\left(\frac{r}{r_s} \right)^\alpha \left[1 - \alpha \ln \left(\frac{r}{r_s} \right) \right] - 1 \right]. \quad (\text{C3})$$

C2 Orbiting: New model (Model A)

If $C = 0$, the derivatives with respect to r_s and α are the same as for the Einasto profile with $C = 0$ (equation C2), and, analogously,

$$\begin{aligned} \frac{d \ln \rho}{d \ln r_t} &= \left(\frac{r}{r_t} \right)^\beta \\ \frac{d \ln \rho}{d \ln \beta} &= \frac{1}{\beta} \left(\frac{r}{r_t} \right)^\beta \left[1 - \beta \ln \left(\frac{r}{r_t} \right) \right]. \end{aligned} \quad (\text{C4})$$

If C is set according to equation (8), we get

$$\begin{aligned} \frac{d \ln \rho}{d \ln r_s} &= 2 \left(\frac{r}{r_s} \right)^\alpha + \left(\frac{r_s}{r_t} \right)^\beta \\ \frac{d \ln \rho}{d \ln \alpha} &= \frac{2}{\alpha} \left[\left(\frac{r}{r_s} \right)^\alpha \left[1 - \alpha \ln \left(\frac{r}{r_s} \right) \right] - 1 \right] \\ \frac{d \ln \rho}{d \ln r_t} &= \left(\frac{r}{r_t} \right)^\beta - \left(\frac{r_s}{r_t} \right)^\beta \\ \frac{d \ln \rho}{d \ln \beta} &= \left(\frac{r}{r_t} \right)^\beta \left[\frac{1}{\beta} - \ln \left(\frac{r}{r_t} \right) \right] - \left(\frac{r_s}{r_t} \right)^\beta \left[\frac{1}{\beta} - \ln \left(\frac{r_s}{r_t} \right) \right]. \end{aligned} \quad (\text{C5})$$

C3 Orbiting: New model (Model B)

When setting $C = 0$, the parameter derivatives for Model B are

$$\begin{aligned} \frac{d \ln \rho}{d \ln r_s} &= 2 \left(\frac{r}{r_s} \right)^\alpha + \left(\frac{r_s}{r_t} \right)^\beta \left(\frac{r}{r_s} \right)^\eta \left[\frac{\beta}{\eta} - 1 \right] \\ \frac{d \ln \rho}{d \ln \alpha} &= \frac{2}{\alpha} \left(\frac{r}{r_s} \right)^\alpha \left[1 - \alpha \ln \left(\frac{r}{r_s} \right) \right] \\ \frac{d \ln \rho}{d \ln r_t} &= \left(\frac{r}{r_t} \right)^\beta - \frac{\beta}{\eta} \left(\frac{r_s}{r_t} \right)^\beta \left(\frac{r}{r_s} \right)^\eta \\ \frac{d \ln \rho}{d \ln \beta} &= \left(\frac{r}{r_t} \right)^\beta \left[\frac{1}{\beta} - \ln \left(\frac{r}{r_t} \right) \right] + \frac{\beta}{\eta} \left(\frac{r_s}{r_t} \right)^\beta \left(\frac{r}{r_s} \right)^\eta \ln \left(\frac{r_s}{r_t} \right) \\ \frac{d \ln \rho}{d \ln \eta} &= \left(\frac{r_s}{r_t} \right)^\beta \left(\frac{r}{r_s} \right)^\eta \left[\ln \left(\frac{r}{r_s} \right) - \frac{1}{\eta} \right]. \end{aligned} \quad (\text{C6})$$

When setting C as in equation (B3), we get

$$\begin{aligned} \frac{d \ln \rho}{d \ln r_s} &= 2 \left(\frac{r}{r_s} \right)^\alpha + \left(\frac{\beta}{\eta} - 1 \right) \left(\frac{r_s}{r_t} \right)^\beta \left[\left(\frac{r}{r_s} \right)^\eta - 1 \right] \\ \frac{d \ln \rho}{d \ln \alpha} &= \frac{2}{\alpha} \left[\left(\frac{r}{r_s} \right)^\alpha \left[1 - \alpha \ln \left(\frac{r}{r_s} \right) \right] - 1 \right] \\ \frac{d \ln \rho}{d \ln r_t} &= \left(\frac{r}{r_t} \right)^\beta - \left(\frac{r_s}{r_t} \right)^\beta \left[\frac{\beta}{\eta} \left[\left(\frac{r}{r_s} \right)^\eta - 1 \right] + 1 \right] \\ \frac{d \ln \rho}{d \ln \beta} &= \left(\frac{r}{r_t} \right)^\beta \left[\frac{1}{\beta} - \ln \left(\frac{r}{r_t} \right) \right] \\ &\quad - \left(\frac{r_s}{r_t} \right)^\beta \left[\frac{1}{\beta} - \ln \left(\frac{r_s}{r_t} \right) \right] \left[\frac{\beta}{\eta} \left[\left(\frac{r}{r_s} \right)^\eta - 1 \right] + 1 \right] \\ \frac{d \ln \rho}{d \ln \eta} &= \frac{1}{\eta} \left(\frac{r_s}{r_t} \right)^\beta \left[\left(\frac{r}{r_s} \right)^\eta \left[\eta \ln \left(\frac{r}{r_s} \right) - 1 \right] + 1 \right]. \end{aligned} \quad (\text{C7})$$

C4 Infalling: New model

We write the derivatives in terms of $Q(r)$ as defined in equation (13),

$$\begin{aligned} \frac{d \ln \rho}{d \ln \delta_1} &= f_m \left[1 - \frac{1}{Q(r)} \left(\frac{\delta_1}{\delta_{\max}} \right)^{1/\zeta} \right] \\ \frac{d \ln \rho}{d \ln s} &= -f_m \frac{s}{Q(r)} \left(\frac{r}{R} \right)^{s/\zeta} \ln \left(\frac{r}{R_{200m}} \right) \\ \frac{d \ln \rho}{d \ln \delta_{\max}} &= f_m \frac{1}{Q(r)} \left(\frac{\delta_1}{\delta_{\max}} \right)^{1/\zeta} \\ \frac{d \ln \rho}{d \ln \zeta} &= f_m \frac{\ln(Q)}{\zeta} \left[\left(\frac{\delta_1}{\delta_{\max}} \right)^{1/\zeta} \ln \left(\frac{\delta_1}{\delta_{\max}} \right) + s \left(\frac{r}{R} \right)^{s/\zeta} \ln \left(\frac{r}{R} \right) \right]. \end{aligned} \quad (\text{C8})$$

All derivatives share the same $f_m \equiv 1 - \rho_m/\rho(r)$ prefactor, which ensures that they vanish at large radii where ρ asymptotically approaches the mean density. This factor is unity when taking the logarithmic derivative of $\rho - \rho_m$, i.e., of only the excess density over the mean. The parameter derivatives of the model without transition sharpness (Section 2.5) are the same but with $\zeta = 1$.

APPENDIX D: DYNAMICAL PROPERTIES

In Section 5.4, we investigated the space of binding energy, whose structure is determined by the positive gravitational potential of a spherical mass distribution. We find the potential by numerically integrating

$$\psi(r) = 4\pi G \left[\frac{M(r)}{r} + \int_r^\infty \rho(r') r' dr' \right]. \quad (\text{D1})$$

For the Einasto profile, we can numerically reproduce the analytical expression for ψ of Retana-Montenegro et al. (2012). Assuming isotropy, the velocity dispersion is found by integrating the Jeans equation,

$$\sigma^2(r) = \frac{1}{\rho(r)} \int_r^\infty \frac{\rho(r') M(r')}{r'^2} dr'. \quad (\text{D2})$$

Analytical expressions for σ exist for some profiles, but they are generally complicated and tend not to extend to Einasto (and other non-power law) forms (e.g., Łokas & Mamon 2001). The distribution function can be found with the expression of Eddington (1916), but this formula involves derivatives of the form $d\rho/d\psi$, which are not easy to compute for arbitrary systems. We follow an easier route by converting to derivatives in r (Binney 1982; Baes & Camps 2021),

$$f(\varepsilon) = \frac{1}{\sqrt{8}\pi^2} \int_{r_\varepsilon}^\infty \frac{g(r)}{\sqrt{\varepsilon - \psi(r)}} dr, \quad (\text{D3})$$

where r_ε is the radius where $\psi(r_\varepsilon) = \varepsilon$ and

$$g(r) \equiv \frac{r^2}{M(r)} \left[\frac{d^2 \rho}{dr^2} + \frac{d\rho}{dr} \left(\frac{2}{r} - \frac{4\pi\rho(r)r^2}{M(r)} \right) \right]. \quad (\text{D4})$$

The problem of finding $f(\varepsilon)$ has now been reduced to computing $d\rho/dr$ and $d^2\rho/dr^2$. We can generally write

$$\frac{d\rho}{dr} = Q(r)\rho \quad \text{and} \quad \frac{d^2\rho}{dr^2} = \rho \left(\frac{dQ}{dr} + Q^2 \right). \quad (\text{D5})$$

For the Einasto profile, we compute

$$Q = -\frac{2}{r} \left(\frac{r}{r_s} \right)^\alpha \quad \text{and} \quad \frac{dQ}{dr} = \frac{Q(\alpha - 1)}{r}. \quad (\text{D6})$$

For Model A, the expressions become somewhat more complicated,

$$Q = -\frac{1}{r} \left[2 \left(\frac{r}{r_s} \right)^\alpha + \left(\frac{r}{r_t} \right)^\beta \right] \quad (\text{D7})$$

and

$$\frac{dQ}{dr} = -\frac{1}{r} \left(Q + \frac{1}{r} \left[2\alpha \left(\frac{r}{r_s} \right)^\alpha + \left(\frac{r}{r_t} \right)^\beta \right] \right). \quad (\text{D8})$$

Finding the equivalent expressions for Model B or for the DK14 fitting function would be tedious but straightforward; we omit them because their properties would be almost indistinguishable from Model A. For all profiles, we have checked that we can recover the input density profile from the distribution function via the integral over energy,

$$\rho(r) = 4\pi \int_0^{\psi(r)} f(\varepsilon) \sqrt{2[\psi(r) - \varepsilon]} d\varepsilon. \quad (\text{D9})$$

This paper has been typeset from a \LaTeX file prepared by the author.